

Nanoscopy of surface polarization with oblique dipole orientations

V. G. M. DUARTE,^{1,2,*} D. A. MIRANDA,³ D. F. P. CUNHA,^{2,5}
 M. I. VASILEVSKIY,^{2,5} N. ASGER MORTENSEN,^{3,4}
 A. J. CHAVES,^{1,5} AND N. M. R. PERES^{2,3,5}

¹*Department of Physics, Aeronautics Institute of Technology, 12228-900, São José dos Campos, SP, Brazil*

²*International Iberian Nanotechnology Laboratory (INL), Av Mestre José Veiga, 4715-330 Braga, Portugal*

³*POLIMA—Center for Polariton-driven Light–Matter Interactions, University of Southern Denmark, Campusvej 55, DK-5230 Odense M, Denmark*

⁴*Danish Institute for Advanced Study, University of Southern Denmark, Campusvej 55, DK-5230 Odense M, Denmark*

⁵*Physics Center of Minho and Porto Universities (CF-UM-UP) and Department of Physics, University of Minho, P-4710-057 Braga, Portugal*

*vgmduarte@gmail.com

Abstract: We present a general electromagnetic description for dipoles confined to surfaces with oblique dipole moment orientations, extending the conventional in-plane (IP) and out-of-plane (OOP) treatments. This description is useful for describing localized polarization in, *e.g.*, van der Waals heterostructures, thin films of molecular aggregates, and metal-dielectric interfaces. The theory is suitable for any material with vanishingly thin thickness relative to the light wavelength, independent of the geometry of the material and the media interfacing it. We apply the formalism to a uniaxial excitonic sheet, covering a large number of two-dimensional (2D) materials and organic thin films. Our theory reveals pairs of polaritonic resonances originating from the IP and OOP components of the excitonic dipole moment. The formalism suggests experimentally accessible signatures of dipole moment orientation, enhanced by near-field probes. This work proposes a unified language for the description of 2D materials, thin films and interfaces with anisotropic dipolar responses.

1. Introduction

The advances of optical microscopy allowed matter to be probed with light at reduced spatial and temporal scales. In particular, scattering-type scanning near-field optical microscopy (s-SNOM) [1] was successfully applied to various systems, including semiconductors [2], organic [3], and biological samples [4], revealing intrinsic properties of matter [5]. For example, the evanescent component of the electric field originated in the s-SNOM tip can be used to excite surface plasmon-polaritons [6], phonon-polaritons [7], and exciton-polaritons [8]. Additionally, synchrotron facilities can be used as a source for synchrotron infrared nanospectroscopy [9].

A natural starting point for studying light-matter interactions is the electric dipole [10], which represents the first-order response of a neutral charge distribution in the presence of an external field. Frenkel excitons, Wannier–Mott excitons, and quantum surface states, hosted respectively by molecules, semiconductors, and metals, interact with light through their electric dipoles. Frenkel excitons are found in organic materials, and have dipole moments oriented following the molecule orientation [11]. Wannier–Mott excitons play the leading role in two-dimensional (2D) materials, and can emit light whose polarization lies within the 2D material plane or perpendicular to it [12]. At last, metallic quantum surface states behave as a series of multipolar corrections to induced charge. These corrections are described through Feibelman’s surface response formalism (SRF) [13], where the parameter d_{\perp} represents the out-of-plane component of the induced dipole near the metal surface, originating from the charge distribution of the quantum surface states.

The description of light interaction with excitons is presented in the seminal work of Hop-

field [14]. However, as pointed elsewhere [15], the dielectric screening reduces both the exciton binding energy and oscillator strengths, making the presence of excitons negligible in most systems [16]. This can be bypassed in nanostructures such as quantum dots [17], or 2D materials [15]. The latter have garnered great attention in recent years due to their optical properties and tunability via environment or layer stacking in van der Waals (vdW) heterostructures. For monolayers of MoS₂ and other transition metal dichalcogenides, the optical properties in the visible range are dominated by the in-plane exciton peak, which is split into two by virtue of spin-orbit coupling. 2D material monolayers also support out-of-plane excitations, but the optical response of those is weaker than that of their in-plane counterparts by a couple orders of magnitude [18]. Nonetheless, the optical response of out-of-plane excitons can be probed by polarization-resolved photoluminescence [12, 19] or near-field spectroscopy [20]. Such out-of-plane excitons can also have their emission enhanced by the Purcell effect through coupling with plasmonic cavities [21]. Furthermore, vdW heterostructures can support interlayer excitons [22], which can possess both static permanent dipoles [23] and an out-of-plane transition dipole component [24]. The static permanent dipoles of interlayer excitons in vdW heterostructures are responsible for an out-of-plane Stark shift [25] and dipole-dipole interactions [23]. When the orbital angular momentum component of the band edges is zero in the direction perpendicular to the 2D plane, the polarization of the photons is perpendicular to the plane [26]. This can be used to design vdW heterostructures with out-of-plane photon emission [27]. Strong out-of-plane photon absorption and emission were observed in monoelemental, binary 2D materials and vdW heterostructures [28].

Besides 2D materials, organic molecules can also exhibit exciton formation. In particular, some molecule species can stack in various geometries and lead to delocalized exciton formation across several molecules [11, 29]. Contrary to 2D materials, organic molecular aggregates are highly disordered, but their excitons have dipole moments with fixed and well defined orientation with respect to the aggregate axis. Compared to their monomer counterparts, these molecular aggregates lead to narrower, redshifted resonances and stronger absorption, associated to the formation of large dipole moments that surpass those found in 2D materials [30, 31] and can lead to exciton-photon coupling potentially reaching the ultrastrong coupling regime [32, 33]. In fact, J-aggregates were one of the first systems to exhibit superradiance under realistic experimental conditions [34]. The description of excitons in such organic materials, as well as their interaction with light, dates back to Kasha's dimer model [35, 36], which describes the fundamental mechanism behind the exciton-exciton coupling and the redshifted resonances. Low-dimensional J-aggregate layers have been employed in films [37] and core-shell nanoparticles [38].

In charged metals, the classical assumption is that the charge is confined to the surface, typically forming an interface with vacuum or a dielectric. However, Feibelman and coworkers proposed a multipole series expansion of the induced charge at an interface [13]. Effectively, the first-order term of this correction corresponds to a dipole-polarized sheet and is responsible for the observation of nonlocal electrodynamic effects in diverse nanophotonics systems [39]. Feibelman's SRF introduces the so-called d -parameters, related to charge and current density centroid positions defined relative to the metal-dielectric interface. They account for charge spill-out, as well as nonlocal screening, leading to corrections in plasmon dispersion that can be measured. For this reason, Feibelman's SRF underpins the current understanding of mesoscopic electrodynamic effects in the field of quantum plasmonics, and provides a perspective into the physics of polarized interfaces between media [40, 41].

The description of dipoles at surfaces typically consider purely in-plane (IP) or out-of-plane (OOP) orientations. Nonetheless, a theory for surface confined dipoles pointing at oblique directions has been made several decades ago, in the context of monolayers of strongly polarized molecules [42–44]. This theory shows that the continuity of the electric field tangential to a surface is broken when an excess polarization perpendicular to the surface is present, an atypical

result that is commonly absent in electrodynamics textbooks [10]. Despite the generality of this discontinuity, until now it has only flourished in the context of higher order nonlinearities [45–47]. The equation for the jump discontinuity of the tangential electric field is in agreement with Feibelman’s SRF, truncated at first-order. The key unifying idea is that an oblique dipole polarization confined to a surface, henceforth denominated as a polarization sheet, generates a singularity in the electric displacement field D_{\perp} perpendicular to the sheet. In this paper, we build upon the theory of Refs. [42–44] with a description of polarization sheets that is independent of the geometry of the sheet and the media interfacing it.

The paper is organized as follows: in Sec. 2 we present the general electromagnetic description of s. Sec. 3 provides the model for investigation of an anisotropic 2D sheet through s-SNOM. In Sec. 4 we consider an excitonic and uniaxial 2D sheet on top of a bulk substrate and examine the resultant reflectivity, surface polariton modes, and s-SNOM spectra. The main conclusions are laid out in Sec. 5.

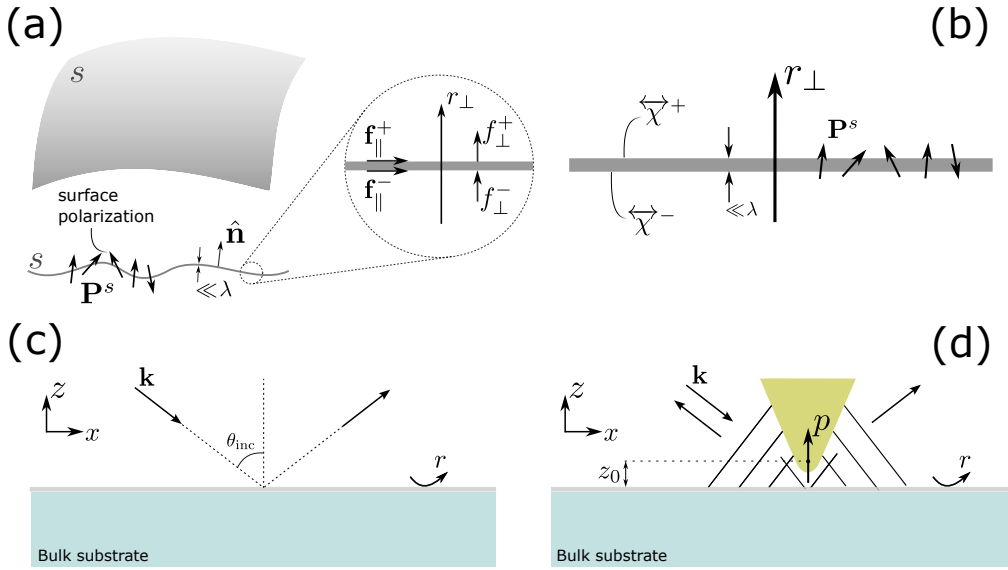


Fig. 1. Schematic representation of a surface S , representing a 2D sheet of arbitrary geometry, and the optical configurations considered in this work. (a) Oblique and lateral views of the surface, showing the surface polarization \mathbf{P}^s , the outward normal $\hat{\mathbf{n}}$, and the sheet thickness (much smaller than the light wavelength λ , thereby allowing the surface treatment). Inset: zoomed-in view of an arbitrary point in the sheet, showing the normal coordinate r_{\perp} taken along the unit vector $\hat{\mathbf{n}}$ and the tangential and normal components of a field \mathbf{f} . (b) Same as the inset in panel (a), indicating the susceptibility tensors $\langle \chi^{\pm} \rangle$ as defined in the text. (c) Geometry considered for optical response calculations. Plane wave fields impinge on the sheet with a wavevector \mathbf{k} and incidence angle θ_{inc} . (d) Same as panel (c), with the addition of a metallic tip to scatter part of the incident light back to a detector in the far-field region. The tip interacts with the sheet generating a point-dipole p , oriented towards the z axis for an elongated tip geometry.

2. Electrodynamics of polarization sheets

It is well established that the continuity of the electric field tangential to a metal-dielectric interface is broken by an OOP surface dipole density π [41], mediated by the parameter d_{\perp} . A similar discontinuity was identified by Heinz [42] and Felderhof & Marowsky [43, 44] in the context of monolayers of strongly polarized molecules, where the tangential electric field

discontinuity is related to the OOP component of the surface polarization field \mathbf{P}^s associated to the monolayer. We will show that these formalisms provide equivalent descriptions of polarization confined to a surface.

2.1. Boundary conditions

We consider a surface s of arbitrary geometry [Fig. 1(a)], hosting charges and currents that generate electromagnetic fields around s . The charge density ρ is related to the current density \mathbf{j} via the continuity equation, written as $\nabla \cdot \mathbf{j} = i\omega\rho$ in the frequency domain. We associate a surface polarization field to this current density via

$$\mathbf{j}(\mathbf{r} + r_\perp \hat{\mathbf{n}}, \omega) = -i\omega \mathbf{P}^s(\mathbf{r}, \omega) \delta(r_\perp), \quad (1)$$

for any point $\mathbf{r} \in s$ and a coordinate r_\perp taken along the direction of the outward normal $\hat{\mathbf{n}}$ relative to s . The charge density may then be written as

$$\rho = -(\nabla \cdot \mathbf{P}^s) \delta(r_\perp) - \mathbf{P}^s \cdot \nabla \delta(r_\perp). \quad (2)$$

The fields generated by the surface s can polarize its vicinities. To this induced polarization we attribute a field \mathbf{P} , from which it follows that the displacement field in the vicinity of s relates to the electric field as $\mathbf{D} = \epsilon_0 \mathbf{E} + \mathbf{P}$. The polarization field \mathbf{P} is indeed the conventional polarization field considered when writing the Maxwell equations in matter, whereas \mathbf{P}^s is a non-classical field attributed to electromagnetic sources confined to a surface.

The Maxwell's equations read

$$\nabla \cdot \mathbf{D} = -(\nabla \cdot \mathbf{P}^s) \delta(r_\perp) - \mathbf{P}^s \cdot \nabla \delta(r_\perp), \quad (3a)$$

$$\nabla \cdot \mathbf{B} = 0, \quad (3b)$$

$$\nabla \times \mathbf{E} = i\omega \mathbf{B}, \quad (3c)$$

$$\nabla \times \mathbf{H} = -i\omega \mathbf{P}^s \delta(r_\perp) - i\omega \mathbf{D}. \quad (3d)$$

Before deriving the BCs, we shall focus on the atypical dipolar term, $-\mathbf{P}^s \cdot \nabla \delta(r_\perp)$. For smooth surfaces s , effects of curvature become negligible in an infinitesimal interval $0^- < r_\perp < 0^+$, and we can use

$$\nabla = \nabla_\parallel + \frac{\partial}{\partial r_\perp} \hat{\mathbf{n}}. \quad (4)$$

Therefore, applying $\int_{0^-}^{0^+} dr_\perp r_\perp (\cdot)$ to Eq. (3a) yields

$$\nabla_\parallel \cdot \int_{0^-}^{0^+} dr_\perp r_\perp \mathbf{D}_\parallel - \int_{0^-}^{0^+} dr_\perp D_\perp = P_\perp^s, \quad (5)$$

where integration by parts was used to simplify the integrals $\int_{0^-}^{0^+} dr_\perp r_\perp \partial / \partial r_\perp (\cdot)$, and \mathbf{f}_\parallel and f_\perp represent the IP and OOP components of a field $\mathbf{f} = \mathbf{f}_\parallel + f_\perp \hat{\mathbf{n}}$. Following the usual procedure of electrodynamics textbooks, integrals of the type $\int_{0^-}^{0^+} dr_\perp \mathbf{f}_\parallel$ will vanish since they are associated to lateral flux across an infinitesimal Gaussian pillbox [10]. Therefore, the first term on the left-hand side of Eq. (5) vanishes, and we are left with

$$\int_{0^-}^{0^+} dr_\perp D_\perp = -P_\perp^s, \quad (6)$$

showing that the integral of the OOP displacement field across the surface is finite, which is only possible if delta function singularities are present in D_\perp . To minimize loss of generality, we assume

that the fields can polarize the surface s back according to $P_{\perp}(\mathbf{r} \in s, \omega) = \epsilon_0 \tilde{\chi}_{\perp}(\omega) E_{\perp}(\mathbf{r} \in s, \omega)$. Then we can write the integral of the polarization field as

$$\int_{0^-}^{0^+} dr_{\perp} P_{\perp} = \epsilon_0 \tilde{\chi}_{\perp} \int_{0^-}^{0^+} dr_{\perp} E_{\perp}. \quad (7a)$$

Concomitantly, Eq. (6) may be rewritten in terms of electric and polarization fields using $D_{\perp} = \epsilon_0 E_{\perp} + P_{\perp}$:

$$\epsilon_0 \int_{0^-}^{0^+} dr_{\perp} E_{\perp} + \int_{0^-}^{0^+} dr_{\perp} P_{\perp} = -P_{\perp}^s. \quad (7b)$$

Rearranging this pair of equations, we get

$$\int_{0^-}^{0^+} dr_{\perp} E_{\perp} = -\frac{P_{\perp}^s}{\epsilon_0(1 + \tilde{\chi}_{\perp})}, \quad (8a)$$

$$P_{\perp}^s + \int_{0^-}^{0^+} dr_{\perp} P_{\perp} = \frac{P_{\perp}^s}{1 + \tilde{\chi}_{\perp}}. \quad (8b)$$

The BCs are obtained applying $\int_{0^-}^{0^+} dr_{\perp}$ to Eqs. (3a–3d). We are left with

$$[D_{\perp}] = -\nabla_{\parallel} \cdot \mathbf{P}_{\parallel}^s, \quad (9a)$$

$$[B_{\perp}] = 0, \quad (9b)$$

$$\hat{\mathbf{n}} \times [\mathbf{E}_{\parallel}] + \nabla_{\parallel} \left(\int_{0^-}^{0^+} dr_{\perp} E_{\perp} \right) \times \hat{\mathbf{n}} = i\omega \int_{0^-}^{0^+} dr_{\perp} B_{\perp}, \quad (9c)$$

$$\hat{\mathbf{n}} \times [\mathbf{H}_{\parallel}] + \nabla_{\parallel} \left(\int_{0^-}^{0^+} dr_{\perp} H_{\perp} \right) \times \hat{\mathbf{n}} = -i\omega \mathbf{P}^s - i\omega \hat{\mathbf{n}} \int_{0^-}^{0^+} dr_{\perp} D_{\perp}, \quad (9d)$$

where $[f] = f^+ - f^-$ is the discontinuity of a (scalar or vector) field f , using the notation $f^{\pm} = f(\mathbf{r} \pm 0^{\pm} \hat{\mathbf{n}})$. The integrals over the magnetic fields B_{\perp} and H_{\perp} , in analogy with Eqs. (6, 8a), go to zero in the absence of an OOP magnetization field singularity in the sheet. Additionally, the terms oriented along $\hat{\mathbf{n}}$ cancel out exactly in the right-hand side of Eq. (9d). Therefore, we obtain the set of BCs

$$[D_{\perp}] = -\nabla_{\parallel} \cdot \mathbf{P}_{\parallel}^s, \quad (10a)$$

$$[B_{\perp}] = 0, \quad (10b)$$

$$[\mathbf{E}_{\parallel}] = -\frac{\nabla_{\parallel} P_{\perp}^{s,\text{eff}}}{\epsilon_0}, \quad (10c)$$

$$[\mathbf{H}_{\parallel}] = -i\omega \mathbf{P}_{\parallel}^s \times \hat{\mathbf{n}}, \quad (10d)$$

where $P_{\perp}^{s,\text{eff}} = P_{\perp}^s / (1 + \tilde{\chi}_{\perp})$ was used.

The BCs (10a–10d) correspond to those obtained by Felderhof & Marowsky [43, 44], although their work considers a homogeneous isotropic medium surrounding the polarization sheet with dielectric constant ϵ , thus implicitly assuming $\tilde{\chi}_{\perp} = \epsilon - 1$. The renormalization of the OOP polarization to $P_{\perp}^{s,\text{eff}} = P_{\perp}^s / (1 + \tilde{\chi}_{\perp})$ highlights the ambiguity of treating the fields \mathbf{P}^s and \mathbf{P} on equal footing. A similar argument is made in Ref. [48], which derives the field of an excess dipole moment in the interface between two dielectric media. The effective OOP polarization $P_{\perp}^{s,\text{eff}}$ is indeed the sum of P_{\perp}^s with the bounded charges induced in an external medium of OOP susceptibility $\tilde{\chi}_{\perp}$, the host medium of the 2D sheet, as Eq. (8b) shows.

Evidently, $\tilde{\epsilon}_{\perp}$ contains the response of the external medium, but could also contain additional sheet polarization effects describable with a finite effective thickness instead of a Dirac's delta, an

ambiguity that is commonly raised in the context of 2D materials [49–51]. The BCs (10a–10d) are in agreement with the BCs obtained for a finite anisotropic sheet embedded in a dielectric environment with permittivity $\tilde{\epsilon}_\perp$ in the OOP direction and a thickness $d \ll \lambda$ (where λ is the wavelength of impinging light) [51]. We can interpret $\nabla_\parallel P_{\perp,\text{eff}}$ in the jump discontinuity of \mathbf{E}_\parallel [Eq. (10c)] as a result of the strong divergence played by $\nabla\delta(r_\perp)$. This divergence shows that, when encapsulating a 2D sheet—using, *e.g.*, hBN [52–56]—, there is a dielectric renormalization of the OOP surface polarization independent of any hybridization between the sheet and the encapsulation material. A complete description of the effective OOP polarization of a 2D sheet thus needs to include both the dielectric screening of the external medium and the interfacial effect of the encapsulation material, but such a task is beyond the scope of this work. Since the intrinsic field \mathbf{P}^s is not experimentally accessible even with the most modern probing techniques, here we work solely with the net field $\mathbf{P}_{\text{eff}}^s = \mathbf{P}_\parallel^s + P_{\perp,\text{eff}}^s \hat{\mathbf{n}}$, which enters the BCs directly.

In the polarization sheet formalism, the surface polarization is related to the electric field through [43]

$$\mathbf{P}_{\text{eff}}^s = \epsilon_0 \overleftrightarrow{\chi}^+ \mathbf{E}^+ + \epsilon_0 \overleftrightarrow{\chi}^- \mathbf{E}^-, \quad (11)$$

thereby establishing a general linear relation, mediated by susceptibility tensors $\overleftrightarrow{\chi}^\pm$. Such a relation can also be obtained in the context of the SRF, using the equations for the OOP surface dipole density $\boldsymbol{\pi}$ and the surface current density $-i\omega\mathbf{P}_\parallel^s$, up to leading order [41]. Here, d_\perp and d_\parallel are Feibelman’s d -parameters. Recognizing that $\boldsymbol{\pi} = \epsilon_0 d_\perp (E_\perp^+ - E_\perp^-) \hat{\mathbf{n}}$ and $-i\omega\mathbf{P}_\parallel^s = i\omega d_\parallel (\mathbf{D}_\parallel^+ - \mathbf{D}_\parallel^-)$, we can write

$$\begin{aligned} \mathbf{P}_{\text{eff}}^s &= -\epsilon_0 d_\parallel (\overleftrightarrow{\epsilon}_\parallel^+ \mathbf{E}_\parallel^+ - \overleftrightarrow{\epsilon}_\parallel^- \mathbf{E}_\parallel^-) + \epsilon_0 d_\perp (E_\perp^+ - E_\perp^-) \hat{\mathbf{n}} \\ &= \epsilon_0 \overleftrightarrow{\chi}_{\text{SRF}}^+ \mathbf{E}^+ + \epsilon_0 \overleftrightarrow{\chi}_{\text{SRF}}^- \mathbf{E}^-, \end{aligned} \quad (12)$$

where $\overleftrightarrow{\chi}_{\text{SRF}}^\pm = \mp d_\parallel \overleftrightarrow{\epsilon}_\parallel^\pm \pm d_\perp \hat{\mathbf{n}} \hat{\mathbf{n}}$, defined in terms of the IP dielectric tensors $\overleftrightarrow{\epsilon}_\parallel^\pm$ of the interfacing media. This concludes the formal equivalence of the SRF to the polarization sheet formalism, with susceptibility tensors defined following the IP optical responses of the metal and dielectric forming the interface. Table 1 summarizes the BCs derived in this Section, together with how they generalize the BCs provided in Refs. [41, 43].

Table 1. Boundary conditions (BCs) of the polarization sheet, using the notation $[f] = f^+ - f^-$, as a function of the sheet’s surface polarization density \mathbf{P}^s . The out-of-plane (OOP) polarization component P_\perp^s is renormalized as $P_{\perp,\text{eff}}^s = P_\perp^s / \tilde{\epsilon}_\perp$ in the presence of an external dielectric medium with OOP permittivity $\tilde{\epsilon}_\perp$ (see main text). For comparison, we show the BCs of Ref. [43], which considers a planar sheet in an isotropic medium (thus $\hat{\mathbf{n}} = \hat{\mathbf{z}}$ and $P_\perp^s = P_z^s$), and Ref. [41], which highlights the BCs with multipolar corrections of Feibelman’s SRF, truncated at leading-order.

This work	Felderhof <i>et al</i> [43]	SRF [41]
$[D_\perp] = -\nabla_\parallel \cdot \mathbf{P}_\parallel^s$	$[D_\perp] = -\nabla_\parallel \cdot \mathbf{P}_\parallel^s$	$[D_\perp] = d_\parallel \nabla_\parallel \cdot [\mathbf{D}_\parallel]$
$[B_\perp] = 0$	$[B_\perp] = 0$	$[B_\perp] = 0$
$[\mathbf{E}_\parallel] = -\nabla_\parallel P_{\perp,\text{eff}}^s / \epsilon_0$	$[\mathbf{E}_\parallel] = -\nabla_\parallel P_z^s / (\epsilon\epsilon_0)$	$[\mathbf{E}_\parallel] = -d_\perp \nabla_\parallel [E_\perp]$
$[\mathbf{H}_\parallel] = -i\omega\mathbf{P}_\parallel^s \times \hat{\mathbf{n}}$	$[\mathbf{H}_\parallel] = -i\omega\mathbf{P}_\parallel^s \times \hat{\mathbf{z}}$	$[\mathbf{H}_\parallel] = i\omega d_\parallel [\mathbf{D}_\parallel] \times \hat{\mathbf{n}}$

2.2. Transfer matrices

In this section, we derive the transfer matrices of the polarization sheet for incidence of linearly polarized light. Planar sheets are considered, but the susceptibility tensors [introduced in Eq. 11]

are assumed biaxial to retain generality:

$$\overleftrightarrow{\chi}^{\pm} = \begin{pmatrix} \chi_{\parallel,1}^{\pm}(\omega) & 0 & 0 \\ 0 & \chi_{\parallel,2}^{\pm}(\omega) & 0 \\ 0 & 0 & \chi_{\perp}^{\pm}(\omega) \end{pmatrix}. \quad (13)$$

The transfer matrices allow for extraction of optical properties such as the reflection and transmission coefficients, as well as for an extensible way of chaining together layered materials with polarization sheets involved.

For the media interfacing the sheet from above (+) and below (-), we assume isotropic dielectric permittivities $\overleftrightarrow{\epsilon}^{\pm} = \epsilon^{\pm} \overleftrightarrow{\mathbf{I}}$ and magnetic permeabilities $\overleftrightarrow{\mu}^{\pm} = \mu^{\pm} \overleftrightarrow{\mathbf{I}}$. Plane waves propagate in these media in the directions $\pm \hat{\mathbf{n}}$. The normal vector $\hat{\mathbf{n}}$ becomes uniform across the entire sheet in the planar case. We define field amplitudes $F_{\pm \hat{\mathbf{n}}}^{\pm}$, such that

$$\mathbf{E}^{\pm} = (F_{+\hat{\mathbf{n}},s}^{\pm} e^{ik_{\perp}r_{\perp}} + F_{-\hat{\mathbf{n}},s}^{\pm} e^{-ik_{\perp}r_{\perp}}) \hat{\mathbf{u}} \quad (14)$$

for s -polarized plane waves, and

$$\mathbf{B}^{\pm} = -(F_{+\hat{\mathbf{n}},p}^{\pm} e^{ik_{\perp}r_{\perp}} + F_{-\hat{\mathbf{n}},p}^{\pm} e^{-ik_{\perp}r_{\perp}}) \hat{\mathbf{u}} \quad (15)$$

for p -polarized plane waves. The unit vector $\hat{\mathbf{u}}$ is defined as $\hat{\mathbf{u}} = \hat{\mathbf{k}}^{\pm} \times \hat{\mathbf{n}}$, with $\mathbf{k}^{\pm} = k^{\pm} \hat{\mathbf{k}}^{\pm} = \mathbf{k}_{\parallel} + k_{\perp}^{\pm} \hat{\mathbf{n}}$ being wavevectors of plane waves propagating on each sheet side.

The transfer matrices of the polarization sheet, defined according to

$$\begin{pmatrix} F_{+\hat{\mathbf{n}},\lambda}^{-} \\ F_{-\hat{\mathbf{n}},\lambda}^{-} \end{pmatrix} = T_{\lambda} \begin{pmatrix} F_{+\hat{\mathbf{n}},\lambda}^{+} \\ F_{-\hat{\mathbf{n}},\lambda}^{+} \end{pmatrix}, \quad (16)$$

are given by the expressions

$$T_s = \frac{1}{2} \begin{pmatrix} 1 + \beta + \eta_s & 1 + \beta - \eta_s \\ 1 - \beta - \eta_s & 1 - \beta + \eta_s \end{pmatrix}, \quad (17a)$$

$$T_p = \frac{\mu^{-}/\mu^{+}}{2(1 - \beta_{\parallel}^{-}\beta_{\parallel}^{-})} \begin{pmatrix} 1 - \beta_{\parallel}^{-} & 1 - \beta_{\perp}^{-} \\ -(1 + \beta_{\parallel}^{-}) & 1 + \beta_{\perp}^{-} \end{pmatrix} \begin{pmatrix} \eta_p(1 - \beta_{\parallel}^{+}) & -\eta_p(1 + \beta_{\perp}^{+}) \\ 1 - \beta_{\parallel}^{+} & 1 + \beta_{\perp}^{+} \end{pmatrix}, \quad (17b)$$

where we defined the auxiliary quantities

$$\eta_s = \mu^{-} k_{\perp}^{+} / (\mu^{+} k_{\perp}^{-}), \quad \eta_p = \epsilon^{-} k_{\perp}^{+} / (\epsilon^{+} k_{\perp}^{-}), \quad (18a)$$

$$\beta = i\omega^2 \mu^{-} (\chi_{\parallel,2}^{+} + \chi_{\parallel,2}^{-}) / (c^2 k_{\perp}^{-}), \quad (18b)$$

$$\beta_{\parallel}^{\pm} = ik_{\perp}^{\pm} \chi_{\parallel,1}^{\pm} / \epsilon^{\pm}, \quad (18c)$$

$$\beta_{\perp}^{\pm} = iq^2 \chi_{\perp}^{\pm} / k_{\perp}^{\pm}. \quad (18d)$$

For a detailed derivation of the transfer matrices (17), the reader is referred to Supplement 1.

2.3. Fresnel coefficients

The Fresnel coefficients of reflection ($r_\lambda = F_{-\hat{\mathbf{n}},\lambda}^-/F_{+\hat{\mathbf{n}},\lambda}^-$) and transmission ($t_\lambda = F_{+\hat{\mathbf{n}},\lambda}^+/F_{+\hat{\mathbf{n}},\lambda}^-$) are obtained by setting $F_{-\hat{\mathbf{n}},\lambda}^+ = 0$:

$$t_s(q, \omega) = \frac{2}{1 + \beta + \eta_s}, \quad (19a)$$

$$r_s(q, \omega) = \frac{1 - \beta - \eta_s}{1 + \beta + \eta_s}, \quad (19b)$$

$$t_p(q, \omega) = \frac{\mu^+}{\mu^-} \frac{2(1 - \beta_{\parallel}^- \beta_{\perp}^-)}{(1 - \beta_{\perp}^-)(1 - \beta_{\parallel}^+) + \eta_p(1 - \beta_{\parallel}^-)(1 - \beta_{\perp}^+)}, \quad (19c)$$

$$r_p(q, \omega) = \frac{(1 + \beta_{\perp}^-)(1 - \beta_{\parallel}^+) - \eta_p(1 + \beta_{\parallel}^-)(1 - \beta_{\perp}^+)}{(1 - \beta_{\perp}^-)(1 - \beta_{\parallel}^+) + \eta_p(1 - \beta_{\parallel}^-)(1 - \beta_{\perp}^+)}. \quad (19d)$$

The reflectance and transmittance follow from $\mathcal{R}_\lambda = |r_\lambda|^2$ and $\mathcal{T}_\lambda = \eta_\lambda |t_\lambda|^2$.

For plane wave incidence coming from the opposite direction ($-\hat{\mathbf{n}}$), it is straightforward to show that the Fresnel coefficients are $r'_\lambda = -r_\lambda$ and $t'_\lambda = t_\lambda$.

3. Near-field spectroscopy of polarization sheets

Near-field spectroscopy allows access to physical properties at sub-wavelength resolution. Several experimental techniques have explored this regime of electrodynamics, with s-SNOM being one of the most successful ones [2]. It consists of shedding a focused laser source on the material under investigation, with a metallic tip in its proximity. The field back-scattered due to laser incidence on the tip-sample system will then be measured by a detector in the far-field region (relative to the tip and sample). By applying a mechanical oscillation to the tip at a frequency Ω , the back-scattered field is modulated in time with components at integer multiples of Ω . These components are probed by a detector in the far-field region, and signatures of tip-sample interaction in the near-field region can be identified through peaks within the demodulated far-field response.

For a tip-sample distance $z_0(t)$ oscillating at frequency Ω , the near-field is $E_{\text{NF}}[z_0(t)] = \sum_{n=-\infty}^{\infty} \sigma_n e^{-in\Omega t}$, where

$$\sigma_n = \frac{1}{T} \int_0^T dt e^{in\Omega t} E_{\text{NF}}[z_0(t)], \quad (20)$$

and $T = 2\pi/\Omega$ is the period of oscillation. Several techniques have been developed to extract the Fourier coefficients σ_n from the signals probed by the detector in an s-SNOM setup [57]. Signatures of near-field interaction are then identified by peaks in the modulus and phase of σ_n .

Describing the near-field interactions of tip and sample in an s-SNOM setup is a challenging task, which has been tackled in works that mix analytical, numerical, and even machine learning techniques [58–69]. To capture the atypical features of the uniaxial 2D sheet within an analytically tractable model, we describe the s-SNOM tip and its interaction with the sheet using a Point-Dipole Model (PDM). The main equations and aspects of the PDM are presented in the following. The notation was simplified by adopting the Cartesian coordinates indicated in Figs. 1(c,d), so that \perp subindices become z subindices, $\mathbf{k}_{\parallel} = \mathbf{q} = q\hat{\mathbf{x}}$, $\hat{\mathbf{n}} = \hat{\mathbf{z}}$, and $r_{\perp} = z$. Additionally, we have $\mu^{\pm} = 1$, $\epsilon^+ = 1$, and $\epsilon^- = \epsilon_{\text{subs}}$ for a sheet between air and a dielectric substrate of permittivity ϵ_{subs} .

We consider a metallic tip brought close to the sheet, aligned to the $\hat{\mathbf{z}}$ axis as displayed in Fig. 1(d). The elongated tip geometry results in a dominant polarization towards the $\hat{\mathbf{z}}$ direction. For a tip in close proximity to the sample and frequencies ω in the near-infrared to visible (NIR-VIS) spectral range, the laser wavelength is much larger than the relevant tip and sample dimensions, and the non-retarded regime can be applied.

The dipole induced in an s-SNOM tip with elongated geometry aligned to the $\hat{\mathbf{z}}$ axis, $\mathbf{p} = p\hat{\mathbf{z}}$, is modeled in the PDM as the response of a sphere of polarizability $\alpha(\omega)$. The z component of the total field acting on the tip may be expanded in terms of an external contribution $E_{0,z}$ and a contribution coming from the dipole's radiation reflected back into itself:

$$E_z = E_{0,z} + Gp, \quad (21a)$$

$$p = \alpha E_z. \quad (21b)$$

Additionally, for a linear homogeneous medium in the absence of additional sources, the external field may be written generically in terms of plane waves propagating in the $+\hat{\mathbf{z}}$ and $-\hat{\mathbf{z}}$ directions. For concreteness, we express this external field as a monochromatic laser, impinging from $z > 0$ with wavevector $\mathbf{k}_{\text{inc}} = q\text{inc}\hat{\mathbf{x}} - k_{z,\text{inc}}\hat{\mathbf{z}}$. An additional contribution is generated from direct reflection into the sample before scattering in the tip. Then,

$$E_{0,z} = E_{\text{inc},z} + rE_{\text{inc},z}e^{2ik_{z,\text{inc}}z_0}, \quad (22)$$

where r is the Fresnel's reflection coefficient of the sheet. Substituting Eqs (21a,22) in Eq. (21b) results in

$$p = \alpha E_{\text{inc},z} \left(1 + re^{2ik_{z,\text{inc}}z_0} \right) + \alpha Gp. \quad (23)$$

Before proceeding, we emphasize the assumptions being made when writing the tip's dipole moment as in Eq. (23): The dipole moment is restricted to $\hat{\mathbf{z}}$ direction as a phenomenological correction of the model to accommodate for the elongated tip geometry. The last term, αGp , includes all tip scattering events, whereas the remaining terms are due to field contributions that exist with or without the presence of the tip. In the following, we proceed to rewrite an expression for the dipole moment solely in terms of the incident field $E_{\text{inc},z}$ and an effective polarizability α_{eff} , which renormalizes the tip to account for the presence of the sheet.

The polarizability may be written in the Clausius–Mossotti form $\alpha(\omega) = 4\pi\epsilon_0 R_{\text{tip}}^3 \frac{\epsilon_{\text{tip}}(\omega) - 1}{\epsilon_{\text{tip}}(\omega) + 2}$, for a radius of curvature R_{tip} and a tip permittivity $\epsilon_{\text{tip}}(\omega)$ [70]. The factor $(1 + re^{2ik_{z,\text{inc}}z_0})$ includes the reflection of the external field on the sheet. The Green's function $G = \omega^2\mu_0 G_{zz}(\mathbf{r}', \mathbf{r}', \omega)$ results from self-reflection of the field radiated by the dipole back into itself. Equation (23) can be rewritten as $p = \alpha_{\text{eff}} (1 + re^{2ik_{z,\text{inc}}z_0}) E_{\text{inc},z}$, where

$$\alpha_{\text{eff}} = \frac{\alpha}{1 - \alpha G} = \frac{1}{\alpha^{-1} - G} \quad (24)$$

is the renormalized polarizability. An expression for G may be derived from the solution of Maxwell's equations for a point-dipole with BCs at the air-sample interface (see Supplement 1):

$$G = \frac{i}{4\pi\epsilon_0} \int_0^\infty dq \frac{q^3}{k_z} e^{2ik_z z_0} r(q, \omega). \quad (25)$$

The back-scattered field is given by the sum of the point-dipole radiation with its reflection on the sheet. Up to leading order, one finds (see Supplement 1)

$$E(\mathbf{R} \rightarrow \infty, \omega) = \frac{ip_{\text{tot}}k e^{ikR}}{2\epsilon_0 R}, \quad (26)$$

where $p_{\text{tot}}(z_0) = p (1 + r(q_{\text{inc}}, \omega) e^{2ik_{z,\text{inc}}z_0})$ to make sure we include both the reflection of the external field and the reflection of the point-dipole's field on the sample, as pointed out by Ref. [62]. We can write

$$p_{\text{tot}}(z_0) = \alpha_{\text{eff}}(z_0) E_{\text{inc},z} (1 + r(q_{\text{inc}}, \omega))^2 + \mathcal{O}(k_{z,\text{inc}}z_0) \quad (27)$$

and the Fourier coefficients (20) are then given by

$$\sigma_n = \frac{ik e^{ikR} E_{\text{inc},z} (1 + r(q_{\text{inc}}, \omega))^2}{2\epsilon_0 RT} \int_0^T dt e^{in\Omega t} \alpha_{\text{eff}}[z_0(t)]. \quad (28)$$

The signal measured in an s-SNOM detector, by means of proper demodulation techniques [57], is proportional to the harmonics σ_n of the back-scattered field, given by Eq. (28) in our PDM. To filter out global phases and unimportant scaling factors, the signal can be normalized as

$$\bar{\sigma}_n = \frac{\sigma_n}{\sigma_{n,\text{subs}}} = \frac{(1 + r(q_{\text{inc}}, \omega))^2}{(1 + r_{\text{subs}}(q_{\text{inc}}))^2} \frac{\int_0^T dt e^{in\Omega t} \alpha_{\text{eff}}[z_0(t)]}{\int_0^T dt e^{in\Omega t} \alpha_{\text{eff,subs}}[z_0(t)]}, \quad (29)$$

where

$$r_{\text{subs}}(q_{\text{inc}}) = \frac{\sqrt{\epsilon_{\text{subs}} - \sin^2(\theta_{\text{inc}})}}{\epsilon_{\text{subs}} \cos(\theta_{\text{inc}})}, \quad (30)$$

is the reflection coefficient of the bare substrate, obtained setting $\chi_{\parallel}^{\pm} = \chi_{\perp}^{\pm} = 0$, and $\alpha_{\text{eff,subs}}$ is the polarizability (24) for $r = r_{\text{subs}}$.

4. Results

In this Section, we simplify the notation by adopting the Cartesian coordinates indicated in Figs. 1(c,d), as in Sec. 3.

To showcase the formalism, we investigate the optical response of excitons confined to a planar 2D sheet. We assume a symmetric uniaxial sheet through $\overleftrightarrow{\chi}^+ = \overleftrightarrow{\chi}^- = \text{diag}(\chi_{\parallel}, \chi_{\parallel}, \chi_{\perp})$, encompassing a large number of 2D systems [39], and use a Lorentzian model for the excitonic contribution to the susceptibility functions, in agreement with the Elliott formula for excitons [71]:

$$\chi_{\parallel,\perp}(\omega) = \frac{f_{\parallel,\perp} \omega_0^2}{\omega_0^2 - \omega^2 - i\omega\gamma}, \quad (31)$$

yielding the usual response of 2D-confined excitonic resonances at frequency ω_0 . The oscillator strengths f_{\parallel} and f_{\perp} modulate the material's response to incident light in the in- and out-of-plane directions, respectively, and the damping parameter γ encompasses all loss sources, thereby modulating the Lorentzian peak's height and width.

We re-parameterize the oscillator strengths as

$$f_{\parallel} = \frac{f_0}{2} \cos^2(\theta_{\text{dip}}), \quad (32a)$$

$$f_{\perp} = f_0 \sin^2(\theta_{\text{dip}}), \quad (32b)$$

so that in- and out-of-plane dipoles may be represented by a single parameter: $\theta_{\text{dip}} = 0^\circ$ (in-plane) and $\theta_{\text{dip}} = 90^\circ$ (out-of-plane). This choice preserves the trace $2f_{\parallel} + f_{\perp} = f_0$. One may view this reparameterization as arising from a set of dipoles confined to a plane, each tilted by a polar angle θ_{dip} away from the plane and uniformly distributed in azimuth [72]. In that picture, f_0 corresponds to the total oscillator strength of the excitonic transition. More generally, however, Eqs. (32) can be regarded simply as a convenient, trace-preserving reparameterization, independent of any particular microscopic interpretation.

Unless stated otherwise, we use $\hbar\omega_0 = 2.1$ eV and $\hbar\gamma = 0.02$ eV, close to the typical values of TMDs and molecular aggregates with excitonic transitions in the VIS range [73, 74]. The oscillator strength f_0 (with units of length in a 2D configuration) is fixed at $f_0 = 2$ nm to match the strong dipole moments of molecular aggregates [72], and the dipole angle is set to $\theta_{\text{dip}} = 20^\circ$ to showcase an oblique dipole orientation.

4.1. Reflectance of a uniaxial 2D sheet

We assume a planar 2D sheet, as depicted in Fig. 1(c). The sheet will first be treated as being standing freely in air ($\epsilon_{\text{subs}} \approx 1$) before considering the case of a real substrate with $\epsilon_{\text{subs}} \neq 1$. Since we are interested in capturing the effect of the OOP polarization component, p -polarization will be considered.

For a free-standing uniaxial 2D sheet with symmetric response ($\overleftrightarrow{\chi}^+ = \overleftrightarrow{\chi}^-$), the reflection coefficient (19b) simplifies to

$$r'_p(q, \omega) = \frac{1}{1 - \beta_{\parallel}} - \frac{1}{1 - \beta_{\perp}}, \quad (33)$$

where $\beta_{\perp} = iq^2\chi_{\perp}/k_z$ and $\beta_{\parallel} = ik_z\chi_{\parallel}$. This suggests that the IP and OOP contributions can cancel each other out. Figures 2(a,c) show the evolution of the reflectance spectrum as a function of incidence angle, for IP and OOP dipole orientations ($\theta_{\text{dip}} = 0^\circ$ and 90° , respectively). For the in-plane reflectance term, maximum dipole-field alignment is achieved when $\theta_{\text{inc}} = 0^\circ$, for which $k = k_z$ and β_{\parallel} stays finite. So the reflectance has a peak at the resonance with broadening mediated by damping. The peak is suppressed as the angle is varied from 0° to 90° , for which k_z goes monotonically from k to 0 and the in-plane dipole component is decoupled.

For the out-of-plane reflectance term, maximum alignment is achieved when $\theta_{\text{inc}} = 90^\circ$. We have $k = q$, $k_z = 0$, and $\beta_{\perp} \rightarrow \infty$. The susceptibility at resonance is given by $f_z\omega_0/(i\gamma)$, therefore β_{\perp} goes to infinity. Far from the resonance, the susceptibility goes asymptotically to zero, but is finite everywhere, so β_{\perp} goes to infinity for any frequency. Hence, both the in-plane and out-of-plane reflectances are resonance-centered peaks, strengthened by field-dipole alignment. The in-plane peak is below 1 and has a narrow shape. The out-of-plane peak saturates at 1 and is severely broadened due to the rapid growth of the factor q^2/k_z in $\beta_{\perp} = iq^2\chi_{\perp}/k_z$. This increase in reflectance when the photon and exciton energies match shows that the photon-exciton interaction deflects the photons away. The shape of the peaks, nonetheless, differs due to an asymmetric decomposition of the field into the in-plane and out-of-plane directions.

Up to now, the reflectance has been analyzed considering a polarization sheet suspended in air. A more common situation, experimentally speaking, would be to place the layer on top of a substrate. Figures 2(b,d) show the reflectance of this new configuration, for in-plane and out-of-plane oriented dipoles. The substrate permittivity used was $\epsilon_{\text{subs}}(\omega) = 2.25$, close to the optical constants of glass and polymers at optical frequency [63]. The substrate, even though lowly reflective, interferes in the reflectance shifting the peaks up slightly for angles close to 0° and largely close to 90° , independent of ω , as the inset in Figs. 2(b,d,e) shows. For such, one may observe that the reflection coefficient of the pure substrate may be written as Eq. (30), canceling out the frequency dependence.

At last, when a substrate is present and the dipole moments have an oblique orientation, both dipole components become present and we may observe destructive interference in the reflectance channel. Fig. 2(e) shows the resulting reflectance spectrum. The double peaks show the interference of dipole components. For visualization, f_0 was increased, representing molecules with stronger dipole moments. To examine the contrast of the peaks compared to the dip at $\omega = \omega_0$, we evaluate the peak visibility, defined as $(|r|_{\text{peak}}^2 - |r|_{\text{dip}}^2)/(|r|_{\text{peak}}^2 + |r|_{\text{dip}}^2)$, as a function of the oscillator strength. For comparison, the typical oscillator strengths of molecular aggregates are close to 2 nm [72]. The oscillator strengths of conventional 2D materials are usually several times smaller [33]. Fig. 2(f) shows that high visibility is achieved only at very large oscillator strengths or angles θ_{inc} approaching grazing incidence, where the in- and out-of-plane reflectance components start interfering.

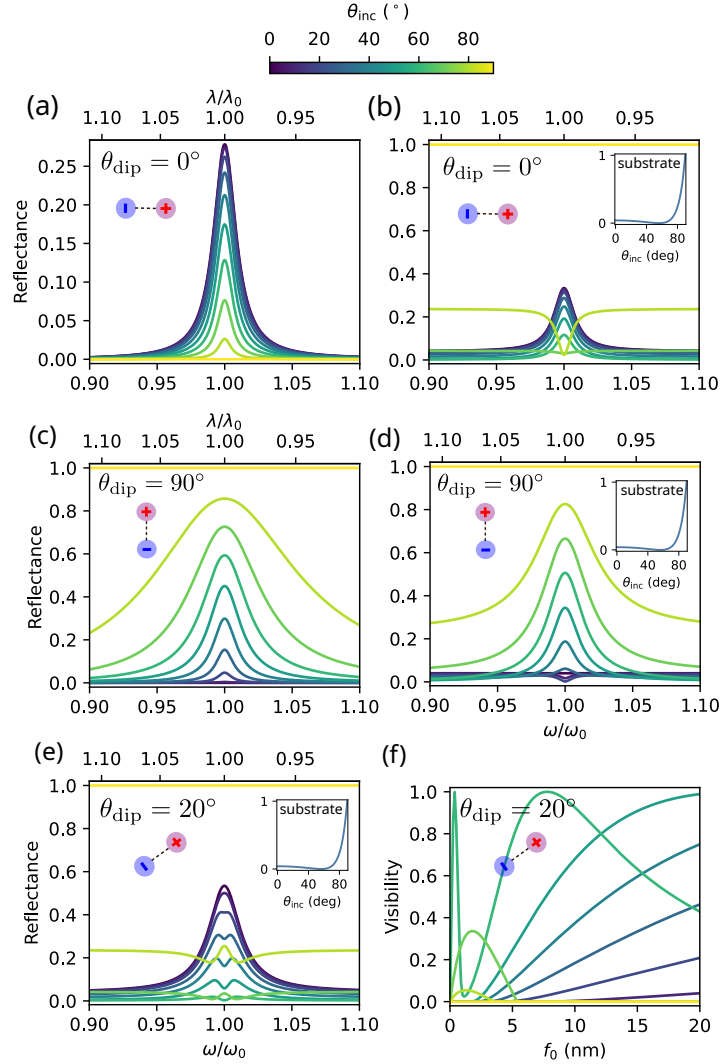


Fig. 2. Reflectance spectrum of excitons confined to a plane, for (a,b) in-plane, (c,d) out-of-plane, and (e) oblique dipole moment orientation. The different curves illustrate the influence of the incidence angle θ_{inc} . The insets in panels (b,d,e) show the reflectance of the substrate, which is a sole function of θ_{inc} . The oscillator strength is $f_0 = 2$ nm in panels (a,b,c,d) and $f_0 = 10$ nm in panel (e) to enhance visualization of the peaks compared to the dip at $\omega = \omega_0$. (f) Visibility, defined as $(|r|_{\text{peak}}^2 - |r|_{\text{dip}}^2) / (|r|_{\text{peak}}^2 + |r|_{\text{dip}}^2)$, as a function of f_0 for different incidence angles.

4.2. Surface polariton modes of a uniaxial 2D sheet

The loss function, defined as $\text{Im}\{r\}$, can be used to infer about surface modes excited by optical means, such as electron energy loss spectroscopy (EELS) [75]. Figs. 3(a,b) show the loss function of the 2D sheet. At the right of the light line, two evanescent stationary modes are present, above and below the excitonic resonance, respectively. The upper mode resembles that of a p -polarized surface polariton in 2D van der Waals materials [76], which only exhibits a polariton branch below the resonance for s -polarized light. Here, by contrast, p -polarized light excites a lower branch with negative group velocity. The insertion of the substrate slightly shifts the branches up

and dampens its peaks, but their qualitative aspect is preserved.

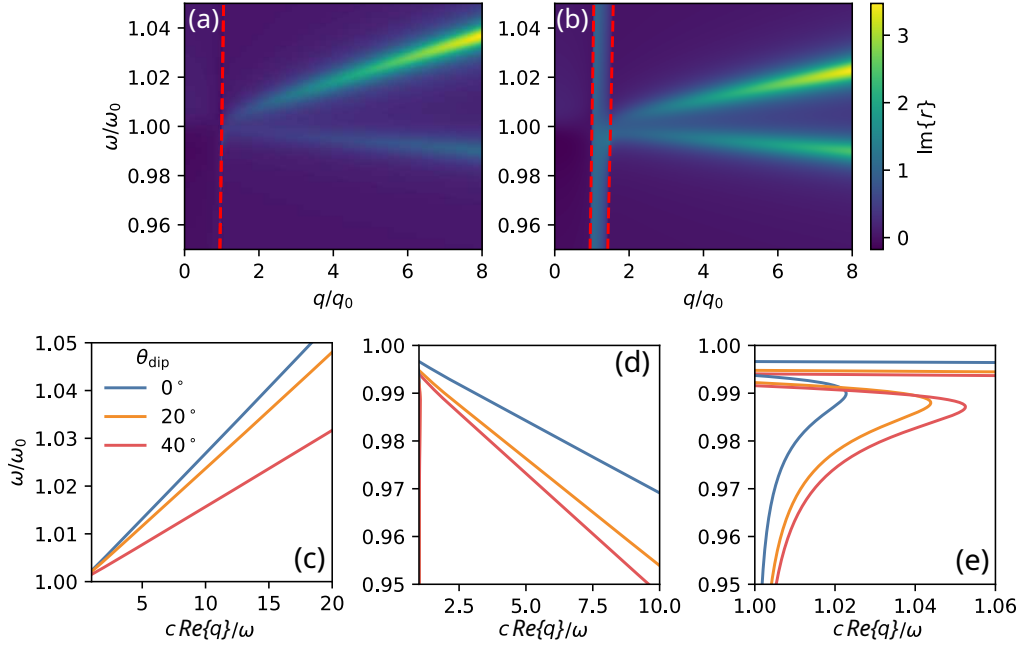


Fig. 3. (a,b) Loss function $\text{Im}\{r\}$ close to the excitonic resonance ($\omega = \omega_0$) of a 2D layer of dipoles (a) suspended in air and (b) on top of a thick substrate layer. Red dashed represents the light lines $q = \omega/c$ and $q = \omega\sqrt{\epsilon_{\text{subs}}}/c$. (c,d,e) Dispersion relation surface modes on a 2D excitonic sheet suspended in air (c) above and (d,e) below the exciton line, for real ω and complex q . Panel (e) shows the modes on a narrower horizontal scale, highlighting the weakly confined modes.

To further examine these surface modes, we solve directly for the poles of the reflection coefficient, which, for a sheet suspended in air, yields $\beta_{\parallel} = 1$ and $\beta_{\perp} = 1$. We get $\kappa_z^t = -1/\chi_t$ and $\kappa_z^{\pm} = (1/\chi_z \pm \sqrt{1/\chi_z^2 - k^2})/2$ (using $k_z = i\kappa_z$). The corresponding modes are $q(\omega) = \sqrt{\omega^2/c^2 + \kappa_z^2}$, and we present the resulting ω vs. $\text{Re}\{q\}$ curves in Figs. 3(c,d,e). We considered real ω and, consequently, complex q . For physical meaningfulness, the results were filtered for $\text{Re}\{\kappa_z\} > 0$, keeping the evanescent behavior away from the sheet. The horizontal axis was normalized by $k = \omega/c$ in order to highlight degree of confinement of the surface modes. An upper branch with positive group velocity (κ_z^t) and a lower branch with negative group velocity (κ_z^+) were obtained. The additional branch (κ_z^-) approaches a free-photon mode, with low confinement since $cq/\omega \sim 1$; hence, it does not form a properly bound surface polariton mode. We further verified the low confinement of the κ_z^- through the ω vs. $\text{Im}\{q\}$ curves, showing that the κ_z^- present lower $\text{Im}\{q\}$ than κ_z^+ across the entire spectrum. In fact, taking into account the group velocity $v_g = d\omega/dq$, we verified that $|\text{Im}\{q\}d\omega/dq| < \gamma/2$ for κ_z^- whereas $|\text{Im}\{q\}d\omega/dq| > \gamma/2$ for κ_z^+ , thereby confirming the low damping of κ_z^- modes.

4.3. *s*-SNOM characterization of oblique dipole orientation

As previously discussed, reflectance experiments lack visibility for electric dipoles with low oscillator strength. Near-field spectroscopy techniques can make dipolar coupling more efficient, allowing for highly visible excitations at subwavelength scale. In this Section, we investigate the *s*-SNOM response of excitons confined to a planar sheet. To allow for direct comparison

with Sec. 4.1, the sheet is placed on top of a substrate with the same optical characterization: $\epsilon_{\text{subs}}(\omega) = 2.25$.

In the following, we examine the modulus $s_n = |\bar{\sigma}_n|$ and phase $\varphi_n = \arg(\bar{\sigma}_n)$ of the normalized field harmonics $\bar{\sigma}_n$. We used numerical integration for the calculation of the effective polarizability (24) and the normalized harmonics (29). Details on how these integrals were performed are given in Supplement 1. There, we show that the integrals in Eq. (29) do not depend on the value of the tapping frequency Ω .

The s-SNOM tip is modeled using a gold sphere of radius $R_{\text{tip}} = 25$ nm, with a Lorentz–Drude model dielectric function that includes corrections in the NIR-VIS range [77]:

$$\epsilon^{\text{tip}}(\omega) = \epsilon^\infty - \frac{\gamma\omega_0^{\text{tip}}}{\omega^2 + i\omega\gamma} + i\left(\frac{\omega_1^{\text{tip}}}{\omega - \Omega_1^{\text{tip}}} + \frac{\omega_1^{\text{tip}*}}{\omega + \Omega_1^{\text{tip}*}}\right), \quad (34)$$

with $\epsilon^\infty = 3.9199$, $\hbar\gamma = 0.0893$ eV, $\hbar\omega_0^{\text{tip}} = 875.79$ eV, $\hbar\omega_1^{\text{tip}} = 3.0701 + 2.9306i$ eV, and $\hbar\Omega_1^{\text{tip}} = 2.7326 - 0.69021i$ eV. For the tip oscillation, we use $z_0(t) = h_0 + A[1 - \cos(\Omega t)]$. Since reducing tip-sample separation enhances the s-SNOM signal [62], we set the closest separation between tip apex and sample to $h_0 = 26$ nm, respecting the geometrical restriction $h_0 > R_{\text{tip}}$. The amplitude A was set to 50 nm in agreement with [63, 68]. We verified that the incidence angle does not play a relevant qualitative or quantitative role in the resulting signals (see Supplement 1), therefore we fix $\theta_{\text{inc}} = 70^\circ$ as it is common to use oblique incidence angles in experiments [2, 78].

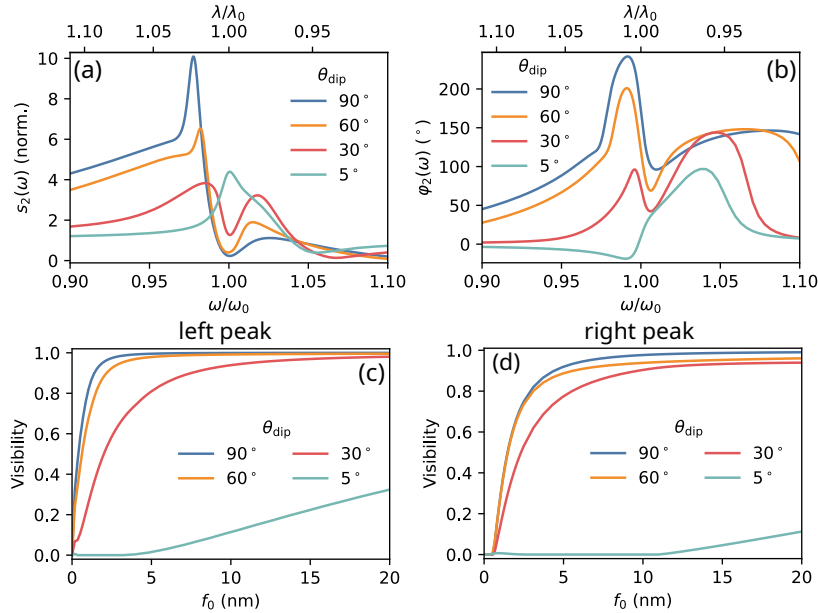


Fig. 4. (a) Modulus and (b) phase of 2nd harmonic demodulated signals of the scattered field, normalized to substrate, for different dipole angles θ_{dip} . (c,d) Visibility of the left (c) and right (d) peaks of panel (a), defined as $(s_{2,\text{peak}} - s_{2,\text{dip}})/(s_{2,\text{peak}} + s_{2,\text{dip}})$.

Figures 4(a) and (b) show the $n = 2$ demodulated harmonics of the 2D excitonic sheet on substrate, for different angles θ_{dip} . Large contrast is observed, with signal peaks reaching up to 10 times the pure substrate signal. This is a consequence not only of the large oscillator strength here considered ($f_0 = 2$ nm) to match those of strongly bounded dipoles in molecular aggregates [72], but also of the substrate being considered. As Fig. 4 already suggested, the two peaks are related to the in- and out-of-plane surface modes mentioned in Sec. 4.2, given by the

poles of the reflection coefficient. As θ_{dip} is varied from 5° to 90° , shifting the molecules away from the sheet’s plane, the peak below ω_0 rises. The peak above ω_0 decreases with increasing θ_{dip} and broadens in width, with its center position shifting towards larger frequencies. The phase spectrum also shows a clear distinction of dipole orientations, however it displays two increasing peaks as the dipole orientation is shifted away from the surface. In Figs. 4(c) and (d) we present the visibility $(s_{2,\text{peak}} - s_{2,\text{dip}})/(s_{2,\text{peak}} + s_{2,\text{dip}})$ as a function of f_0 , showing much larger peak-to-dip contrast at lower oscillator strengths when compared to those of the bare reflectance measurements [Fig. 2(f)]. This result reveals the potential of s-SNOM to identify and characterize dipole moment orientations with higher resolution and contrast.

As a last remark, we would like to bring attention to the shape of the s_2 curves in Fig. 4(a). The $\theta_{\text{dip}} = 90^\circ$ presents a shape that is quite resembling of a Fano resonance, with a dip close to $s_2 = 0$ at the discrete dipolar resonance $\omega = \omega_0$. As punctuated in related works [63, 79], this indicates an interference of the dipolar surface with the tip in analogy with that of a discrete state with a continuum of states in quantum mechanics. Indeed, we verified that, due to renormalization of the tip’s polarizability by interaction with the dipolar surface, a Fano-like resonance can be verified through the spectral features of the effective polarizability [Eq. (24)], which are present at $\theta_{\text{dip}} = 90^\circ$ (see Supplement 1). The in-plane dipole component does not couple efficiently with the tip’s point-dipole, however its correspondent s_2 curve shape also displays a slight asymmetry due to influence of the substrate. The s_2 shapes for oblique oriented dipoles are a consequence of phase interference between the in-plane- and out-of-plane-projected field components, which, as Sec. 4.1 suggested, generates a mix of destructive and constructive interferences in the spectral range of interest. For this reason, the s_2 curve shapes for $0 < \theta_{\text{dip}} < 90^\circ$ are quite more complicated, despite preserving the peak trends as already discussed.

5. Conclusion

To account for the out-of-plane dipole orientation, Felderhof’s formalism of linear polarization sheets was reviewed and generalized to an arbitrary sheet geometry and interfacing media. By doing so, we developed a flexible model that provides a unified theoretical language. It applies to 2D sheets arising either from surface-confined excitonic resonances in molecular layers and vdW heterostructures or from plasmonic resonances at metal–dielectric interfaces described by Feibelman’s SRF. Our formalism provides a stepping stone into the development of a complete mesoscopic description of surface polarization fluctuations in 2D-confined regions, bridging the gap between macro- and microscopic electrodynamics.

We demonstrated the characterization of average dipole orientation in a layer of excitonic transition dipoles confined to two-dimensions. By examining a planar 2D sheet on a substrate of weak reflectivity, we were able to show distinct reflectance peaks clearly associated with exciton-polaritons originating from to in- and out-of-plane dipole contributions, which interfere destructively when the dipole moments are obliquely oriented. These peaks achieve higher visibility when employing near-field techniques — here exemplified through a s-SNOM setup—, which generates Fano-like resonances that capture the effect of surface modes in the sheet.

Funding. São Paulo Research Foundation (2023/14231-6, 2024/05040-5); Independent Research Fund Denmark (2032-00045B). Portuguese Foundation for Science and Technology (UID/04650/2025, PTDC/FIS-MAC/2045/2021). Danish National Research Foundation (Project No. DNRF165).

Acknowledgments. V. G. M. D. acknowledges a PhD. Scholarship from the São Paulo Research Foundation (FAPESP), Processes No. 2023/14231-6 and 2024/05040-5. N. M. R. P. and N. A. M. acknowledge the Independent Research Fund Denmark (grant no. 2032-00045B). N. M. R. P. also acknowledges support from the Portuguese Foundation for Science and Technology (FCT) in the framework of the Strategic Funding UID/04650/2025 and by the project PTDC/FIS-MAC/2045/2021. The Center for Polariton-driven Light–Matter Interactions (POLIMA) is funded by the Danish National Research Foundation (Project No. DNRF165).

Disclosures. The authors declare no conflicts of interest.

Data Availability. All data supporting the findings of this study are available within the article.

Supplemental document. See Supplement 1 for supporting content.

References

- [1] D. Richards, A. Zayats, F. Keilmann, and R. Hillenbrand, “Near-field microscopy by elastic light scattering from a tip,” *Philos. Trans. Royal Soc. London. Ser. A: Math. Phys. Eng. Sci.* **362**, 787–805 (2004).
- [2] X. Chen, D. Hu, R. Mescall, *et al.*, “Modern scattering-type scanning near-field optical microscopy for advanced material research,” *Adv. Mater.* **31**, 1804774 (2019).
- [3] V. J. Rao, M. Matthiesen, K. P. Goetz, *et al.*, “AFM-IR and IR-SNOM for the characterization of small molecule organic semiconductors,” *The J. Phys. Chem. C* **124**, 5331–5344 (2020).
- [4] V. Subramaniam, A. K. Kirsch, and T. M. Jovin, “Cell biological applications of scanning near-field optical microscopy (SNOM).” *Cell. Mol. Biol. (Noisy-le-Grand, France)* **44**, 689–700 (1998).
- [5] J. M. Atkin, S. Berweger, A. C. Jones, and M. B. Raschke, “Nano-optical imaging and spectroscopy of order, phases, and domains in complex solids,” *Adv. Phys.* **61**, 745–842 (2012).
- [6] A. V. Zayats and I. I. Smolyaninov, “Near-field photonics: surface plasmon polaritons and localized surface plasmons,” *J. Opt. A: Pure Appl. Opt.* **5**, S16 (2003).
- [7] A. J. Huber, N. Ocelic, and R. Hillenbrand, “Local excitation and interference of surface phonon polaritons studied by near-field infrared microscopy,” *J. Microsc.* **229**, 389–395 (2008).
- [8] F. Hu, Y. Luan, J. Speltz, *et al.*, “Imaging propagative exciton polaritons in atomically thin WSe₂ waveguides,” *Phys. Rev. B* **100**, 121301 (2019).
- [9] I. D. Barcelos, H. A. Bechtel, C. J. S. de Matos, *et al.*, “Probing polaritons in 2D materials with synchrotron infrared nanospectroscopy,” *Adv. Opt. Mater.* **8**, 1901091 (2020).
- [10] J. D. Jackson, *Classical electrodynamics* (John Wiley & Sons, 2021).
- [11] J. L. Bricks, Y. L. Sifominskii, I. D. Panas, and A. P. Demchenko, “Fluorescent J-aggregates of cyanine dyes: basic research and applications review,” *Methods Appl. Fluoresc.* **6**, 012001 (2017).
- [12] G. Wang, C. Robert, M. M. Glazov, *et al.*, “In-plane propagation of light in transition metal dichalcogenide monolayers: Optical selection rules,” *Phys. Rev. Lett.* **119**, 047401 (2017).
- [13] P. J. Feibelman, “Surface electromagnetic fields,” *Prog. Surf. Sci.* **12**, 287–407 (1982).
- [14] J. J. Hopfield, “Theory of the contribution of excitons to the complex dielectric constant of crystals,” *Phys. Rev.* **112**, 1555 (1958).
- [15] G. Wang, A. Chernikov, M. M. Glazov, *et al.*, “Colloquium: Excitons in atomically thin transition metal dichalcogenides,” *Rev. Mod. Phys.* **90**, 021001 (2018).
- [16] H. Haug and S. W. Koch, *Quantum theory of the optical and electronic properties of semiconductors* (world scientific, 2009).

- [17] T. Takagahara, “Effects of dielectric confinement and electron-hole exchange interaction on excitonic states in semiconductor quantum dots,” *Phys. Rev. B* **47**, 4569–4584 (1993).
- [18] I. Guilhon, M. Marques, L. K. Teles, *et al.*, “Out-of-plane excitons in two-dimensional crystals,” *Phys. Rev. B* **99**, 161201 (2019).
- [19] Y. Zhou, G. Scuri, D. S. Wild, *et al.*, “Probing dark excitons in atomically thin semiconductors via near-field coupling to surface plasmon polaritons,” *Nat. Nanotechnol.* **12**, 856–860 (2017).
- [20] Y. Kim and J. Kim, “Near-field optical imaging and spectroscopy of 2D-TMDs,” *Nanophotonics* **10**, 3397–3415 (2021).
- [21] X. Bao, X. Wu, Y. Ke, *et al.*, “Giant out-of-plane exciton emission enhancement in two-dimensional indium selenide via a plasmonic nanocavity,” *Nano Lett.* **23**, 3716–3723 (2023).
- [22] S. Feng, A. J. Campbell, M. Brotons-Gisbert, *et al.*, “Highly tunable ground and excited state excitonic dipoles in multilayer 2H-MoSe₂,” *Nat. Commun.* **15**, 4377 (2024).
- [23] W. Li, X. Lu, S. Dubey, *et al.*, “Dipolar interactions between localized interlayer excitons in van der Waals heterostructures,” *Nat. Mater.* **19**, 624–629 (2020).
- [24] H. Yu, G.-B. Liu, and W. Yao, “Brightened spin-triplet interlayer excitons and optical selection rules in van der Waals heterobilayers,” *2D Mater.* **5**, 035021 (2018).
- [25] L. A. Jauregui, A. Y. Joe, K. Pistunova, *et al.*, “Electrical control of interlayer exciton dynamics in atomically thin heterostructures,” *Science* **366**, 870–875 (2019).
- [26] D. J. Terry, V. Zólyomi, M. Hamer, *et al.*, “Infrared-to-violet tunable optical activity in atomic films of gase, inse, and their heterostructures,” *2D Mater.* **5**, 041009 (2018).
- [27] N. Ubrig, E. Ponomarev, J. Zultak, *et al.*, “Design of van der Waals interfaces for broad-spectrum optoelectronics,” *Nat. Mater.* **19**, 299–304 (2020).
- [28] T.-H. Wu and K.-H. Lin, “Out-of-plane optical absorption, emission and carrier dynamics in layered materials,” *2D Mater.* **12**, 042007 (2025).
- [29] F. Würthner, T. E. Kaiser, and C. R. Saha-Möller, “J-aggregates: From serendipitous discovery to supramolecular engineering of functional dye materials,” *Angewandte Chemie Int. Ed.* **50**, 3376–3410 (2011).
- [30] K. Misawa, K. Minoshima, H. Ono, and T. Kobayashi, “Giant static dipole moment change on electronic excitation in highly oriented J-aggregates,” *Chem. Phys. Lett.* **220**, 251–256 (1994).
- [31] T. Kobayashi, “Giant static dipole moment in pseudoisocyanine j-aggregate with a hierarchical structure,” *Mol. Cryst. Liq. Cryst. Sci. Technol. Sect. A. Mol. Cryst. Liq. Cryst.* **314**, 1–11 (1998).
- [32] P. Forn-Díaz, L. Lamata, E. Rico, *et al.*, “Ultrastrong coupling regimes of light-matter interaction,” *Rev. Mod. Phys.* **91**, 025005 (2019).
- [33] V. G. M. Duarte, A. J. Chaves, and N. M. R. Peres, “Organic-inorganic polaritonics: Linking Frenkel and Wannier-Mott excitons,” *Phys. Rev. B* **111**, L201404 (2025).

- [34] F. C. Spano and S. Mukamel, “Superradiance in molecular aggregates,” *The J. Chem. Phys.* **91**, 683–700 (1989).
- [35] M. Kasha, “Energy transfer mechanisms and the molecular exciton model for molecular aggregates,” *Radiat. Res.* **20**, 55–70 (1963).
- [36] M. Kasha, *Molecular Excitons in Small Aggregates* (Springer US, Boston, MA, 1976), pp. 337–363.
- [37] J. H. Kim, T. Schembri, D. Bialas, *et al.*, “Slip-stacked J-aggregate materials for organic solar cells and photodetectors,” *Adv. Mater.* **34** (2021).
- [38] N. T. Fofang, T.-H. Park, O. Neumann, *et al.*, “Plexcitonic nanoparticles: Plasmon–exciton coupling in nanoshell–J-aggregate complexes,” *Nano Lett.* **8**, 3481–3487 (2008).
- [39] F. Monticone, N. A. Mortensen, A. I. Fernández-Domínguez, *et al.*, “Nonlocality in photonic materials and metamaterials: roadmap,” *Opt. Mater. Express* **15**, 1544 (2025).
- [40] T. Christensen, W. Yan, A.-P. Jauho, *et al.*, “Quantum Corrections in Nanoplasmonics: Shape, Scale, and Material,” *Phys. Rev. Lett.* **118**, 157402 (2017).
- [41] Y. Yang, D. Zhu, W. Yan, *et al.*, “A general theoretical and experimental framework for nanoscale electromagnetism,” *Nature* **576**, 248–252 (2019).
- [42] T. F. Heinz, “Nonlinear optics of surfaces and adsorbates,” Ph.d. thesis, University of California at Berkeley (1983).
- [43] B. U. Felderhof and G. Marowsky, “Linear optics of polarization sheets,” *Appl. Phys. B* **43**, 161–166 (1987).
- [44] B. U. Felderhof and G. Marowsky, “Electromagnetic radiation from a polarization sheet located at an interface between two media,” *Appl. Phys. B* **44**, 11–17 (1987).
- [45] J. Löbau and K. Wolfrum, “Sum-frequency spectroscopy in total internal reflection geometry: signal enhancement and access to molecular properties,” *J. Opt. Soc. Am. B* **14**, 2505 (1997).
- [46] K. Nireekshan Reddy, P. Y. Chen, A. I. Fernández-Domínguez, and Y. Sivan, “Revisiting the boundary conditions for second-harmonic generation at metal-dielectric interfaces,” *J. Opt. Soc. Am. B* **34**, 1824 (2017).
- [47] E. Dremetsika and P. Kockaert, “Enhanced optical Kerr effect method for a detailed characterization of the third-order nonlinearity of two-dimensional materials applied to graphene,” *Phys. Rev. B* **96** (2017).
- [48] M. A. Mohamed, E. F. Kuester, M. Picket-May, and C. L. Holloway, “The field of an electric dipole and the polarizability of a conducting object embedded in the interface between dielectric materials,” *Prog. In Electromagn. Res. B* **16**, 1–20 (2009).
- [49] T. Tian, D. Scullion, D. Hughes, *et al.*, “Electronic polarizability as the fundamental variable in the dielectric properties of two-dimensional materials,” *Nano Lett.* **20**, 841–851 (2020).
- [50] A. Yadav, C. M. Acosta, G. M. Dalpian, and O. I. Malyi, “First-principles investigations of 2D materials: Challenges and best practices,” *Matter* **6**, 2711–2734 (2023).
- [51] B. Majérus, E. Dremetsika, M. Lobet, *et al.*, “Electrodynamics of two-dimensional materials: Role of anisotropy,” *Phys. Rev. B* **98**, 125419 (2018).

- [52] X. Han, J. Lin, J. Liu, *et al.*, “Effects of hexagonal boron nitride encapsulation on the electronic structure of few-layer MoS₂,” *The J. Phys. Chem. C* **123**, 14797–14802 (2019).
- [53] K. Y. Ma, M. Kim, and H. S. Shin, “Large-area hexagonal boron nitride layers by chemical vapor deposition: Growth and applications for substrates, encapsulation, and membranes,” *Accounts Mater. Res.* **3**, 748–760 (2022).
- [54] S. Pace, L. Martini, D. Convertino, *et al.*, “Synthesis of large-scale monolayer 1T′-MoTe₂ and its stabilization via scalable hBN encapsulation,” *ACS Nano* **15**, 4213–4225 (2021).
- [55] J. I.-J. Wang, Y. Yang, Y.-A. Chen, *et al.*, “Electronic transport of encapsulated graphene and WSe₂ devices fabricated by pick-up of prepatterned hBN,” *Nano Lett.* **15**, 1898–1903 (2015).
- [56] F. Ye, Q. Liu, B. Xu, *et al.*, “Ultra-high interfacial thermal conductance via double hBN encapsulation for efficient thermal management of 2d electronics,” *Small* **19**, 2205726 (2023).
- [57] G. Dai, Z. Yang, G. Geng, *et al.*, “Signal detection techniques for scattering-type scanning near-field optical microscopy,” *Appl. Spectrosc. Rev.* **53**, 806–835 (2018).
- [58] Z. Li, B. Gu, and G. Yang, “Modified self-consistent approach applied in near-field optics for mesoscopic surface defects,” *Phys. Rev. B* **55**, 10883–10894 (1997).
- [59] B. Knoll and F. Keilmann, “Enhanced dielectric contrast in scattering-type scanning near-field optical microscopy,” *Opt. Commun.* **182**, 321–328 (2000).
- [60] R. Hillenbrand, B. Knoll, and F. Keilmann, “Pure optical contrast in scattering-type scanning near-field microscopy,” *J. Microsc.* **202**, 77–83 (2001).
- [61] J. N. Walford, J. A. Porto, R. Carminati, *et al.*, “Influence of tip modulation on image formation in scanning near-field optical microscopy,” *J. Appl. Phys.* **89**, 5159–5169 (2001).
- [62] A. Cvitkovic, N. Ocelic, and R. Hillenbrand, “Analytical model for quantitative prediction of material contrasts in scattering-type near-field optical microscopy,” *Opt. Express* **15**, 8550–8565 (2007).
- [63] J. Aizpurua, T. Taubner, F. J. García de Abajo, *et al.*, “Substrate-enhanced infrared near-field spectroscopy,” *Opt. Express* **16**, 1529–1545 (2008).
- [64] B. Hauer, A. P. Engelhardt, and T. Taubner, “Quasi-analytical model for scattering infrared near-field microscopy on layered systems,” *Opt. Express* **20**, 13173–13188 (2012).
- [65] X. Gao and A. Eisfeld, “Near-field spectroscopy of nanoscale molecular aggregates,” *The J. Phys. Chem. Lett.* **9**, 6003–6010 (2018).
- [66] X. Chen, R. Ren, and M. Liu, “Validity of machine learning in the quantitative analysis of complex scanning near-field optical microscopy signals using simulated data,” *Phys. Rev. Appl.* **15**, 014001 (2021).
- [67] S. Nayak, F. Zheng, and A. Eisfeld, “Near-field scanning optical microscopy of molecular aggregates: The role of light polarization,” *The J. Chem. Phys.* **155**, 134701 (2021).
- [68] I. Pascual Robledo, C. Maciel-Escudero, M. Schnell, *et al.*, “Theoretical description of infrared near-field spectroscopy of in- and out-of-plane molecular vibrations in thin layers,” *ACS Photonics* **12**, 3782–3793 (2025).

- [69] O. Garrity, I. Niehues, A. Bergmann-Iwe, *et al.*, “Characterizing interlayer excitons by spectral signature in scattering visible near-field microscopy,” *The J. Phys. Chem. Lett.* **16**, 6960–6967 (2025).
- [70] B. Amorim, P. A. D. Gonçalves, M. I. Vasilevskiy, and N. M. R. Peres, “Impact of graphene on the polarizability of a neighbour nanoparticle: A dyadic Green’s function study,” *Appl. Sci.* **7**, 1158 (2017).
- [71] R. J. Elliott, “Intensity of optical absorption by excitons,” *Phys. Rev.* **108**, 1384–1389 (1957).
- [72] D. Cunha, M. Barreiro, J. Gama, *et al.*, “Exciton-polaritons support by organic and hybrid semiconductor platforms,” in *2025 25th Anniversary International Conference on Transparent Optical Networks (ICTON)*, (2025), pp. 1–4.
- [73] W. Zhang, J.-B. You, J. Liu, *et al.*, “Steering room-temperature plexcitonic strong coupling: A diexcitonic perspective,” *Nano Lett.* **21**, 8979–8986 (2021).
- [74] J. Ye, Y. Pan, G. Liu, *et al.*, “Strong coupling between a plasmon mode and multiple different exciton states,” *Sci. China Physics, Mech. & Astron.* **66**, 244212 (2023).
- [75] P. A. D. Gonçalves and N. M. R. Peres, *An Introduction to Graphene Plasmonics* (World Scientific, 2016).
- [76] F. Ferreira, A. J. Chaves, N. M. R. Peres, and R. M. Ribeiro, “Excitons in hexagonal boron nitride single-layer: a new platform for polaritonics in the ultraviolet,” *J. Opt. Soc. Am. B* **36**, 674–683 (2019).
- [77] H. S. Sehmi, W. Langbein, and E. A. Muljarov, “Optimizing the Drude-Lorentz model for material permittivity: Method, program, and examples for gold, silver, and copper,” *Phys. Rev. B* **95**, 115444 (2017).
- [78] T. Neuman, P. Alonso-González, A. Garcia-Etxarri, *et al.*, “Mapping the near fields of plasmonic nanoantennas by scattering-type scanning near-field optical microscopy,” *Laser & Photonics Rev.* **9**, 637–649 (2015).
- [79] E. G. Bortchagovsky and U. C. Fischer, “On the modulation of optical transmission spectra of thin dye layers by a supporting medium,” *The J. Chem. Phys.* **117**, 5384–5392 (2002).

Nanoscopy of surface polarization with oblique dipole orientations: supplemental document

This supplemental document provides the detailed mathematical and physical derivations that underpin the theoretical framework presented in the main article, “Nanoscopy of surface polarization with arbitrary dipole orientations”. We present the complete, explicit derivation of the Transfer Matrices for a uniaxial polarization sheet. This includes the application of Maxwell’s equations, Fourier transforms, and boundary conditions to solve for both s and p light polarizations, which formally link the field amplitudes on either side of the polarization sheet. Furthermore, we detail the full mathematical implementation of the PDM, including the formal calculations for the s -SNOM signal. This involves the derivation and calculation of the self-reflected field of the tip’s point-dipole, necessary to capture the near-field tip-sample interaction. We also include auxiliary figures and technical discussions, such as the maximum contrast achievable at large incidence angles.

1. TRANSFER MATRICES OF PLANAR AND ANISOTROPIC POLARIZATION SHEETS

The boundary conditions summarized in Table 1 of the main text reduce to

$$\epsilon^+ E_{\perp}^+ - \epsilon^- E_{\perp}^- = -\overleftarrow{\chi}_{\parallel}^+ \nabla_{\parallel} \cdot \mathbf{E}_{\parallel}^+ - \overleftarrow{\chi}_{\parallel}^- \nabla_{\parallel} \cdot \mathbf{E}_{\parallel}^-, \quad (\text{S1a})$$

$$B_z^+ - B_z^- = 0, \quad (\text{S1b})$$

$$\mathbf{E}_{\parallel}^+ - \mathbf{E}_{\parallel}^- = -\chi_{\perp}^+ \nabla_{\parallel} E_{\perp}^+ - \chi_{\perp}^- \nabla_{\parallel} E_{\perp}^-, \quad (\text{S1c})$$

$$\frac{\mathbf{B}_{\parallel}^+}{\mu^+} - \frac{\mathbf{B}_{\parallel}^-}{\mu^-} = -\frac{i\omega}{c^2} \overleftarrow{\chi}_{\parallel}^+ \mathbf{E}_{\parallel}^+ \times \hat{\mathbf{n}} - \frac{i\omega}{c^2} \overleftarrow{\chi}_{\parallel}^- \mathbf{E}_{\parallel}^- \times \hat{\mathbf{n}}, \quad (\text{S1d})$$

where $\overleftarrow{\chi}_{\parallel}^{\pm} = \text{diag}(\chi_{\parallel,1}^{\pm}, \chi_{\parallel,2}^{\pm})$. Inside the media $+$ and $-$, the Maxwell’s equations can be compactly represented as

$$\nabla \times \mathbf{E}^{\pm} = i\omega \mathbf{B}^{\pm}, \quad (\text{S2a})$$

$$\nabla \times \mathbf{B}^{\pm} = -\frac{i\omega \mu^{\pm} \epsilon^{\pm}}{c^2} \mathbf{E}^{\pm} \quad (\text{S2b})$$

since the divergence equations $\nabla \cdot \mathbf{E}^{\pm} = 0$ and $\nabla \cdot \mathbf{B}^{\pm} = 0$ follow directly by applying $\nabla \cdot$ on Eqs. (S2). The application of the Fourier transforms

$$f(\mathbf{r}_{\parallel}) = \int \frac{d^2 \mathbf{q}}{(2\pi)^2} e^{i\mathbf{q} \cdot \mathbf{r}_{\parallel}} \tilde{f}(\mathbf{q}) \quad (\text{S3a})$$

follows by substituting $f \rightarrow \tilde{f}$ ($f = D, B, E, H$) and $\nabla_{\parallel} \rightarrow i\mathbf{q}$. In the following, we omit the tilde notation and consider the solutions of Eqs. (S1) and (S2) for s - and p -light polarizations.

A. s polarization

Using Eq. (S2a) and $E^{\pm} = F_{+\hat{\mathbf{n}},s}^{\pm} e^{ik_{\perp} r_{\perp}} + F_{-\hat{\mathbf{n}},s}^{\pm} e^{-ik_{\perp} r_{\perp}}$, we get

$$\mathbf{B}^{\pm} = \frac{1}{i\omega} (i\mathbf{q} + \partial_{\perp} \hat{\mathbf{n}}) \times (E^{\pm} (\hat{\mathbf{n}} \times \hat{\mathbf{q}})) = -\frac{q}{\omega} E^{\pm} \hat{\mathbf{n}} + \frac{1}{i\omega} \partial_{\perp} E^{\pm} \hat{\mathbf{q}}. \quad (\text{S4})$$

The fields given by Eqs. (S4) already satisfy Eq. (S2b). Substituting them on the boundary conditions (S1) yields

$$E^+ - E^- = 0, \quad (\text{S5a})$$

$$\frac{1}{i\omega} \left(\frac{\partial_{\perp} E^+}{\mu^+} - \frac{\partial_{\perp} E^-}{\mu^-} \right) = -\frac{i\omega}{c^2} (\chi_{\parallel,2}^+ E^+ + \chi_{\parallel,2}^- E^-). \quad (\text{S5b})$$

In Eqs. (S5), it is implicitly assumed that z is evaluated at the position of the sheet, $z = z_{ps}$. Defining $E_{\pm\hat{n}}^{\pm} = F_{\pm\hat{n}}^{\pm} e^{\pm ik_{zj} z_{ps}}$, we can rewrite these equations as

$$E_{+\hat{n}}^{-} + E_{-\hat{n}}^{-} = E_{+\hat{n}}^{+} + E_{-\hat{n}}^{+}, \quad (\text{S6a})$$

$$\frac{ik_{\perp}^{+}}{\mu^{+}}(E_{+\hat{n}}^{+} - E_{-\hat{n}}^{+}) - \frac{ik_{\perp}^{-}}{\mu^{-}}(E_{+\hat{n}}^{-} - E_{-\hat{n}}^{-}) = \frac{\omega^2}{c^2} \chi_{\parallel,1}^{+} (E_{+\hat{n}}^{+} + E_{-\hat{n}}^{+}) + \frac{\omega^2}{c^2} \chi_{\parallel,2}^{-} (E_{+\hat{n}}^{-} + E_{-\hat{n}}^{-}) \quad (\text{S6b})$$

Substituting the first equation on the second, we get

$$E_{+\hat{n}}^{-} + E_{-\hat{n}}^{-} = E_{+\hat{n}}^{+} + E_{-\hat{n}}^{+}, \quad (\text{S7a})$$

$$\frac{ik_{\perp}^{+}}{\mu^{+}}(E_{+\hat{n}}^{+} - E_{-\hat{n}}^{+}) - \frac{ik_{\perp}^{-}}{\mu^{-}}(E_{+\hat{n}}^{-} - E_{-\hat{n}}^{-}) = \frac{\omega^2}{c^2} (E_{+\hat{n}}^{-} + E_{-\hat{n}}^{-}) (\chi_{\parallel,2}^{+} + \chi_{\parallel,2}^{-}). \quad (\text{S7b})$$

Rearranging,

$$E_{+\hat{n}}^{-} + E_{-\hat{n}}^{-} = E_{+\hat{n}}^{+} + E_{-\hat{n}}^{+}, \quad (\text{S8a})$$

$$\left(\frac{\omega^2}{c^2} (\chi_{\parallel,2}^{+} + \chi_{\parallel,2}^{-}) + \frac{ik_{\perp}^{-}}{\mu^{-}} \right) E_{+\hat{n}}^{-} + \left(\frac{\omega^2}{c^2} (\chi_{\parallel,2}^{+} + \chi_{\parallel,2}^{-}) - \frac{ik_{\perp}^{-}}{\mu^{-}} \right) E_{-\hat{n}}^{-} = \frac{ik_{\perp}^{+}}{\mu^{+}} E_{+\hat{n}}^{+} - \frac{ik_{\perp}^{+}}{\mu^{+}} E_{-\hat{n}}^{+} \quad (\text{S8b})$$

Multiplying both sides of the second equation by ik_{\perp}^{-}/μ^{-} ,

$$E_{+\hat{n}}^{-} + E_{-\hat{n}}^{-} = E_{+\hat{n}}^{+} + E_{-\hat{n}}^{+}, \quad (\text{S9a})$$

$$(\beta - 1) E_{+\hat{n}}^{-} + (\beta + 1) E_{-\hat{n}}^{-} = -\eta_{\mu} E_{+\hat{n}}^{+} + \eta_{\mu} E_{-\hat{n}}^{+}, \quad (\text{S9b})$$

where $\beta = i\omega^2 k_{\perp}^{-} (\chi_{\parallel,2}^{-} + \chi_{\parallel,2}^{+}) / (c^2 k_{\perp}^{-})$ and $\eta_{\mu} = \mu^{-} k_{\perp}^{+} / \mu^{+} k_{\perp}^{-}$. In matrix form, these equations can be written as

$$\begin{pmatrix} 1 & 1 \\ \beta - 1 & \beta + 1 \end{pmatrix} \begin{pmatrix} E_{+\hat{n}}^{-} \\ E_{-\hat{n}}^{-} \end{pmatrix} = \begin{pmatrix} 1 & 1 \\ -\eta_{\mu} & \eta_{\mu} \end{pmatrix} \begin{pmatrix} E_{+\hat{n}}^{+} \\ E_{-\hat{n}}^{+} \end{pmatrix}, \quad (\text{S10})$$

which reduces to

$$\begin{pmatrix} E_{+\hat{n}}^{-} \\ E_{-\hat{n}}^{-} \end{pmatrix} = \frac{1}{2} \begin{pmatrix} 1 + \beta + \eta_{\mu} & 1 + \beta - \eta_{\mu} \\ 1 - \beta - \eta_{\mu} & 1 - \beta + \eta_{\mu} \end{pmatrix} \begin{pmatrix} E_{+\hat{n}}^{+} \\ E_{-\hat{n}}^{+} \end{pmatrix}. \quad (\text{S11})$$

B. p polarization

For p -polarization, we can write $\mathbf{B}^{\pm} = -B^{\pm} \hat{\mathbf{u}}$, where

$$B^{\pm} = F_{+\hat{n}}^{\pm} e^{ik_{zj} z} + F_{-\hat{n}}^{\pm} e^{-ik_{zj} z}, \quad (\text{S12a})$$

with generic amplitudes $F_{+\hat{n}}^{\pm}$ and $F_{-\hat{n}}^{\pm}$. Using Eq. (S2b), we get

$$\mathbf{E}^{\pm} = -\frac{c^2}{i\omega\mu^{\pm}\epsilon^{\pm}} (i\mathbf{q} + \partial_{\perp} \hat{\mathbf{n}}) \times (B^{\pm} (\hat{\mathbf{n}} \times \hat{\mathbf{q}})) = -\frac{c^2 q B^{\pm}}{\omega\mu^{\pm}\epsilon^{\pm}} \hat{\mathbf{n}} + \frac{c^2}{i\omega\mu^{\pm}\epsilon^{\pm}} \partial_{\perp} B^{\pm} \hat{\mathbf{q}}. \quad (\text{S12b})$$

The fields given by Eqs. (S12) already satisfy Eq. (S2a). Substituting them on the boundary conditions (S1) yields

$$-\frac{c^2 q B^{+}}{\omega\mu^{+}} + \frac{c^2 q B^{-}}{\omega\mu^{-}} = -\frac{qc^2 \chi_{\parallel,1}^{+}}{\omega\mu^{+}\epsilon^{-}} \partial_{\perp} B^{+} - \frac{qc^2 \chi_{\parallel,1}^{-}}{\omega\mu^{-}\epsilon^{-}} \partial_{\perp} B^{-}, \quad (\text{S13a})$$

$$\frac{c^2}{i\omega\mu^{+}\epsilon^{+}} \partial_{\perp} B^{+} - \frac{c^2}{i\omega\mu^{-}\epsilon^{-}} \partial_{\perp} B^{-} = \frac{ic^2 q^2 \chi_{\perp,1}^{+} B^{+}}{\omega\mu^{+}\epsilon^{+}} + \frac{ic^2 q^2 \chi_{\perp,1}^{-} B^{-}}{\omega\mu^{-}\epsilon^{-}}. \quad (\text{S13b})$$

In Eqs. (S13), it is implicitly assumed that $z = z_{ps}$. Defining $B_{\pm\hat{n}}^{\pm} = F_{\pm\hat{n}}^{\pm} e^{\pm ik_{zj} z_{ps}}$ we can rewrite these equations as

$$\frac{k_{\perp}^{+}}{\mu^{+}\epsilon^{+}} (B_{+\hat{n}}^{+} - B_{-\hat{n}}^{+}) - \frac{k_{\perp}^{-}}{\mu^{-}\epsilon^{-}} (B_{+\hat{n}}^{-} - B_{-\hat{n}}^{-}) = \frac{iq^2 \chi_{\perp,1}^{+}}{\mu^{+}\epsilon^{+}} (B_{+\hat{n}}^{+} + B_{-\hat{n}}^{+}) + \frac{iq^2 \chi_{\perp,1}^{-}}{\mu^{-}\epsilon^{-}} (B_{+\hat{n}}^{-} + B_{-\hat{n}}^{-}) \quad (\text{S14a})$$

$$\frac{B_{+\hat{n}}^{+} + B_{-\hat{n}}^{+}}{\mu^{+}} - \frac{B_{+\hat{n}}^{-} + B_{-\hat{n}}^{-}}{\mu^{-}} = \frac{ik_{\perp}^{+} \chi_{\parallel,1}^{+}}{\mu^{+}\epsilon^{+}} (B_{+\hat{n}}^{+} - B_{-\hat{n}}^{+}) + \frac{ik_{\perp}^{-} \chi_{\parallel,2}^{-}}{\mu^{-}\epsilon^{-}} (B_{+\hat{n}}^{-} - B_{-\hat{n}}^{-}) \quad (\text{S14b})$$

Rearranging,

$$\begin{aligned} \left(\frac{iq^2\chi_{\perp}^-}{\mu^-\epsilon^-} + \frac{k_{\perp}^-}{\mu^-\epsilon^-} \right) B_{+\hat{\mathbf{n}}}^- + \left(\frac{iq^2\chi_{\perp}^-}{\mu^-\epsilon^-} - \frac{k_{\perp}^-}{\mu^-\epsilon^-} \right) B_{-\hat{\mathbf{n}}}^- &= \left(\frac{k_{\perp}^+}{\mu^+\epsilon^+} - \frac{iq^2\chi_{\perp}^+}{\mu^+\epsilon^+} \right) B_{+\hat{\mathbf{n}}}^+ \\ &\quad - \left(\frac{k_{\perp}^+}{\mu^+\epsilon^+} + \frac{iq^2\chi_{\perp}^+}{\mu^+\epsilon^+} \right) B_{-\hat{\mathbf{n}}}^+, \end{aligned} \quad (\text{S15a})$$

$$\begin{aligned} \left(\frac{ik_{\perp}^-\chi_{\parallel,1}^-}{\mu^-\epsilon^-} + \frac{1}{\mu^-} \right) B_{+\hat{\mathbf{n}}}^- + \left(\frac{1}{\mu^-} - \frac{ik_{\perp}^-\chi_{\parallel,1}^-}{\mu^-\epsilon^-} \right) B_{-\hat{\mathbf{n}}}^- &= \left(\frac{1}{\mu^+} - \frac{ik_{\perp}^+\chi_{\parallel,1}^+}{\mu^+\epsilon^+} \right) B_{+\hat{\mathbf{n}}}^+ \\ &\quad + \left(\frac{1}{\mu^+} + \frac{ik_{\perp}^+\chi_{\parallel,1}^+}{\mu^+\epsilon^+} \right) B_{-\hat{\mathbf{n}}}^+. \end{aligned} \quad (\text{S15b})$$

Multiplying both sides of the first equation by $\mu^-\epsilon^-/k_{\perp}^-$, and the second equation, by μ^- , we get

$$(\beta_{\perp}^- + 1) B_{+\hat{\mathbf{n}}}^- + (\beta_{\perp}^- - 1) B_{-\hat{\mathbf{n}}}^- = \frac{\mu^-}{\mu^+} \eta_{\epsilon} (1 - \beta_{\perp}^+) B_{+\hat{\mathbf{n}}}^+ - \frac{\mu^-}{\mu^+} \eta_{\epsilon} (1 + \beta_{\perp}^+) B_{-\hat{\mathbf{n}}}^+, \quad (\text{S16a})$$

$$(1 + \beta_{\parallel}^-) B_{+\hat{\mathbf{n}}}^- + (1 - \beta_{\parallel}^-) B_{-\hat{\mathbf{n}}}^- = \frac{\mu^-}{\mu^+} (1 - \beta_{\parallel}^+) B_{+\hat{\mathbf{n}}}^+ + \frac{\mu^-}{\mu^+} (1 + \beta_{\parallel}^+) B_{-\hat{\mathbf{n}}}^+, \quad (\text{S16b})$$

where $\beta_{\perp}^{\pm} = iq^2\chi_{\perp}^{\pm}/(k_{\perp}^{\pm})$, $\beta_{\parallel}^{\pm} = ik_{\perp}^{\pm}\chi_{\parallel,1}^{\pm}/\epsilon^{\pm}$, and $\eta_{\epsilon} = \epsilon^-k_{\perp}^+ / (\epsilon^+k_{\perp}^-)$. In matrix form, these equations can be written as

$$\begin{pmatrix} \beta_{\perp}^- + 1 & \beta_{\perp}^- - 1 \\ 1 + \beta_{\parallel}^- & 1 - \beta_{\parallel}^- \end{pmatrix} \begin{pmatrix} B_{+\hat{\mathbf{n}}}^- \\ B_{-\hat{\mathbf{n}}}^- \end{pmatrix} = \frac{\mu^-}{\mu^+} \begin{pmatrix} \eta_{\epsilon}(1 - \beta_{\perp}^+) & \eta_{\epsilon}(1 + \beta_{\perp}^+) \\ 1 - \beta_{\parallel}^+ & 1 + \beta_{\parallel}^+ \end{pmatrix} \begin{pmatrix} B_{+\hat{\mathbf{n}}}^+ \\ B_{-\hat{\mathbf{n}}}^+ \end{pmatrix}, \quad (\text{S17})$$

which reduces to

$$\begin{pmatrix} B_{+\hat{\mathbf{n}}}^- \\ B_{-\hat{\mathbf{n}}}^- \end{pmatrix} = \frac{\mu^-/\mu^+}{2(1 - \beta_{\parallel}^-\beta_{\perp}^-)} \begin{pmatrix} 1 - \beta_{\parallel}^- & 1 - \beta_{\perp}^- \\ -(1 + \beta_{\parallel}^-) & 1 + \beta_{\perp}^- \end{pmatrix} \begin{pmatrix} \eta_{\epsilon}(1 - \beta_{\perp}^+) & \eta_{\epsilon}(1 + \beta_{\perp}^+) \\ 1 - \beta_{\parallel}^+ & 1 + \beta_{\parallel}^+ \end{pmatrix} \begin{pmatrix} B_{+\hat{\mathbf{n}}}^+ \\ B_{-\hat{\mathbf{n}}}^+ \end{pmatrix}. \quad (\text{S18})$$

2. POINT-DIPOLE MODEL FOR ANISOTROPIC POLARIZATION SHEETS

The key idea of the PDM is to describe the tip-scattered radiation as the field of a dipole excited in a dielectric sphere by an external field in the quasi-static approximation, which is justified in a regime where retardation effects can be neglected. In the following, we relate the tip's point-dipole with the incoming external field via a polarizability function, making sure to include self-interaction effects due to reflection of the tip's radiation on the polarization sheet. The resulting expressions for the tip's point-dipole field \mathbf{E}_{tip} and its reflection on the sample \mathbf{E}_{ref} are then used to calculate the total back-scattered field $\mathbf{E} = \mathbf{E}_{\text{tip}} + \mathbf{E}_{\text{ref}}$ as seen from a detector in the far-field region.

A. Self-interaction of the tip

In the PDM, the s-SNOM tip is modeled as a point-dipole with polarizability α , placed at a distance z_0 from the sample [Fig. 1(d) of the main text]. For elongated tips, the polarization is dominant along the $\hat{\mathbf{z}}$ direction, resulting in a dipole moment $\mathbf{p} = p\hat{\mathbf{z}}$. The polarizability α is modeled by first treating the tip as a dielectric sphere. Then, if some external field with wavelength $\lambda \gg R_{\text{tip}}$ —with R_{tip} being the radius of the dielectric sphere—impinges on this tip, the dipole moment distribution may be treated as point-like. The resultant dipole moment up to leading order is [1]

$$p = \alpha E_{0z} + \alpha G p, \quad (\text{S19a})$$

$$\alpha = 4\pi\epsilon_0 R_{\text{tip}}^3 \frac{\epsilon_{\text{tip}} - 1}{\epsilon_{\text{tip}} + 2}, \quad (\text{S19b})$$

where $E_{0z} = \mathbf{E}_0 \cdot \hat{\mathbf{z}}$ and \mathbf{E}_0 is the external field at the dipole's position, with reflections on the sample included. The G term comes from reflection of the dipole's radiated field back into itself due to interaction with the sample. Eq. (S19a) may be rewritten as

$$p = \frac{\alpha}{1 - \alpha G} E_{0z} = \alpha_{\text{eff}} E_{0z}. \quad (\text{S20})$$

The field component E_{0z} may be written as $E_{0z} = E_{\text{inc}} \sin \theta_{\text{inc}} e^{-ik_{\perp} z_0} + E_{\text{ref}} \sin \theta_{\text{inc}} e^{ik_{\perp} z_0} = E_{\text{inc},z} (1 + r'_p(q, \omega) e^{2ik_{\perp} z_0})$, with $E_{\text{inc},z} = E_{\text{inc}} \sin(\theta_{\text{inc}}) e^{-ik_{\perp} z_0}$. Therefore,

$$p = \alpha_{\text{eff}} \left(1 + r'_p(q, \omega) e^{2ik_{\perp} z_0} \right) E_{\text{inc},z}. \quad (\text{S21})$$

In the following, we derive expressions for G , and proceed by showing how the back-scattered field can be expressed in terms of p .

B. Self-reflected Green's function of a point-dipole near a polarization sheet

For a point-dipole carrying a dipole moment $p(t) = p e^{-i\omega t}$ in vacuum, centered at the origin, one can write the Faraday equation

$$\nabla \times \mathbf{E} = i\omega \mathbf{B}, \quad (\text{S22})$$

which, after applying $\nabla \times$ on both sides, becomes

$$-\nabla^2 \mathbf{E} + \nabla \nabla \cdot \mathbf{E} = i\omega \nabla \times \mathbf{B} = i\omega \mu_0 \mathbf{j} + \frac{\omega^2}{c^2} \mathbf{E}, \quad (\text{S23})$$

where the Ampere-Maxwell equation

$$\nabla \times \mathbf{B} = \mu_0 \mathbf{j} - \frac{i\omega}{c^2} \mathbf{E} \quad (\text{S24})$$

was used, with $\mathbf{B} = \mu_0 \mathbf{H}$. Applying $\nabla \cdot$ on both sides of Eq. (S24) one gets

$$\nabla \cdot \mathbf{E} = \frac{c^2 \mu_0 \nabla \cdot \mathbf{j}}{i\omega} = \frac{\nabla \cdot \mathbf{j}}{i\omega \epsilon_0}, \quad (\text{S25})$$

which can be substituted back on Eq. (S23) to arrive at

$$\nabla^2 \mathbf{E} + \frac{\omega^2}{c^2} \mathbf{E} = -i\omega \mu_0 \mathbf{j} + \frac{\nabla \nabla \cdot \mathbf{j}}{i\omega \epsilon_0} = -i\omega \mu_0 \left(1 + \frac{\nabla \nabla \cdot}{\omega^2 / c^2} \right) \mathbf{j}, \quad (\text{S26})$$

known as the inhomogeneous Helmholtz equation.

The current density may be related with the dipole moment through $\mathbf{j}(\mathbf{r}, t) = \partial_t (\mathbf{p} e^{-i\omega t} \delta(\mathbf{r})) = -i\omega \mathbf{p} e^{-i\omega t} \delta(\mathbf{r})$. The harmonic time-dependence will be omitted, as all fields will assume the same harmonic time dependence, already considered for derivation of Eq. (S26). In momentum space, the inhomogeneous Helmholtz equation for the current of a point-dipole reads

$$\left(\frac{\omega^2}{c^2} - k^2 \right) \mathbf{E} = -\omega^2 \mu_0 \left(1 - \frac{\mathbf{k} \mathbf{k} \cdot}{\omega^2 / c^2} \right) \mathbf{p}, \quad (\text{S27})$$

which can be readily solved for \mathbf{E} and transformed back to real space:

$$\mathbf{E}(\mathbf{r}) = \omega^2 \mu_0 \int \frac{d^3 \mathbf{k}}{(2\pi)^3} e^{i\mathbf{k} \cdot \mathbf{r}} \frac{\frac{\mathbf{k} \mathbf{k} \cdot}{k_0^2} - 1}{k_0^2 - k^2} \mathbf{p}, \quad (\text{S28})$$

where $k_0 = \omega/c$.

For the purposes of this work, it suffices to consider a dipole moment oriented along $\hat{\mathbf{z}}$, $\mathbf{p} = p \hat{\mathbf{z}}$. The integral on k_{\perp} of Eq. (S28) then becomes solvable by means of contour integration:

$$\begin{aligned} \mathbf{E}(\mathbf{q}, z) &= \omega^2 \mu_0 p \int_{-\infty}^{\infty} \frac{dk_{\perp}}{2\pi} e^{ik_{\perp} z} \frac{\mathbf{q} k_{\perp} / k_0^2 + (k_{\perp}^2 / k_0^2 - 1) \hat{\mathbf{z}}}{k_0^2 - k^2} \\ &= \omega^2 \mu_0 p \begin{cases} \oint \frac{dk_{\perp}}{2\pi} e^{ik_{\perp} z} \frac{\mathbf{q} k_{\perp} / k_0^2 + (k_{\perp}^2 / k_0^2 - 1) \hat{\mathbf{z}}}{k_0^2 - k^2 + i0^+}, z > 0 \\ - \oint \frac{dk_{\perp}}{2\pi} e^{ik_{\perp} z} \frac{\mathbf{q} k_{\perp} / k_0^2 + (k_{\perp}^2 / k_0^2 - 1) \hat{\mathbf{z}}}{k_0^2 - k^2 + i0^+}, z < 0 \end{cases} \\ &= i\omega^2 \mu_0 p \begin{cases} e^{ik_{z0} z} \frac{\mathbf{q} k_{z0} / k_0^2 - q^2 \hat{\mathbf{z}} / k_0^2}{2k_{z0}}, z > 0 \\ -e^{-ik_{z0} z} \frac{-\mathbf{q} k_{z0} / k_0^2 - q^2 \hat{\mathbf{z}} / k_0^2}{2k_{z0}}, z < 0 \end{cases} ; k_{z0} = \sqrt{k_0^2 - q^2} \\ &= \frac{ip}{\epsilon_0} e^{ik_{z0}|z|} \frac{\mathbf{q} k_{z0} - \text{sign}(z) q^2 \hat{\mathbf{z}}}{2k_{z0}}. \end{aligned} \quad (\text{S29})$$

Therefore, the z -dependence of the point-dipole field is analogous to that of a plane wave. The index 0 in k_{z0} will be omitted in the following. The total field of a point-dipole in the vicinity of a polarization sheet may be written as

$$\mathbf{E}_1(\mathbf{q}, z) = \frac{ip}{\epsilon_0} e^{ik_{\perp}|z|} \frac{\mathbf{q}k_{\perp} - \text{sign}(z)q^2\hat{\mathbf{z}}}{2k_{\perp}} + \mathbf{E}_{r0}(\mathbf{q})e^{ik_{\perp}z}, \quad (\text{S30})$$

$$\mathbf{E}_2(\mathbf{q}, z) = \mathbf{E}_{t0}(\mathbf{q})e^{-ik_{\perp}z}, \quad (\text{S31})$$

where the indices $j = 1, 2$ are introduced to represent the field above and below the sheet, respectively, and z_0 is the distance from the point-dipole to a polarization sheet placed at $z = -z_0$. The Faraday equation, applied to the point-dipole term in the field \mathbf{E}_1 , gives

$$\begin{aligned} \mathbf{B}_i &= \frac{p}{2\omega\epsilon_0} (i\mathbf{q} + \partial_{\perp}\hat{\mathbf{z}}) \times \left(e^{ik_{\perp}|z|} \frac{\mathbf{q}k_{\perp} - \text{sign}(z)q^2\hat{\mathbf{z}}}{k_{\perp}} \right) \\ &= \frac{ip\omega}{2c^2\epsilon_0 k_{\perp}} \text{sign}(z) e^{ik_{\perp}|z|} (\hat{\mathbf{z}} \times \hat{\mathbf{q}}), \end{aligned} \quad (\text{S32})$$

which, at $z = -z_0$, is an incident field of amplitude $A'_1 = -ip\omega/(2c^2\epsilon_0 k_{\perp})$. For a reflection coefficient defined as $r'_p = (F_{-\hat{\mathbf{n}}p}^- e^{-ik_{\perp}z_0})/(F_{+\hat{\mathbf{n}}p}^- e^{ik_{\perp}z_0})$, this results in a reflected magnetic field

$$\mathbf{B}_r = -r'_p e^{2ik_{\perp}z_0} \frac{ip\omega}{2c^2\epsilon_0 k_{\perp}} e^{ik_{\perp}z} (\hat{\mathbf{z}} \times \hat{\mathbf{q}}), \quad (\text{S33})$$

with an associated electric field obtained through Ampere-Maxwell's equation:

$$\begin{aligned} \mathbf{E}_r &= \mathbf{E}_{r0} e^{ik_{\perp}z} = -r'_p e^{-2ik_{\perp}z_0} \frac{ic^2}{\omega} \frac{ipq\omega}{2c^2\epsilon_0 k_{\perp}} (i\mathbf{q} + \partial_{\perp}\hat{\mathbf{z}}) \times \left(e^{ik_{\perp}z} (\hat{\mathbf{z}} \times \hat{\mathbf{q}}) \right) \\ &= r'_p e^{2ik_{\perp}z_0} \frac{ipq}{2\epsilon_0 k_{\perp}} e^{ik_{\perp}z} (q\hat{\mathbf{z}} - k_{\perp}\hat{\mathbf{q}}). \end{aligned} \quad (\text{S34})$$

The z -component of such reflected field, evaluated at the point-dipole's position $\mathbf{r}' = \mathbf{0}$, may be written as $G(\mathbf{r}', \mathbf{r}', \omega)p$ where

$$G = \frac{i}{4\pi\epsilon_0} \int_{-\infty}^{\infty} dq e^{2ik_{\perp}z_0} \frac{q^3}{k_{\perp}} r'_p(q, \omega) \quad (\text{S35})$$

is the self-reflected Green's function of the point-dipole near the polarization sheet. In fact, this result is more general and holds for a point-like sphere ($R_{\text{dip}} \ll \lambda$) near any interface under TM-polarized light illumination, provided that the reflection coefficient $r(q, \omega)$ is adapted accordingly. Not surprisingly, this result was also obtained by [1–3] under similar argumentation.

C. Back-scattered field evaluated at the far-field region

The total back-scattered field is the sum of the field radiated by the tip's point-dipole p and by the sample:

$$\begin{aligned} \mathbf{E}(\mathbf{r}, \omega) &= \mathbf{E}_{\text{tip}}(\mathbf{r}_{\parallel}, z > z_0, \omega) + \mathbf{E}_{\text{ref}}(\mathbf{r}, \omega) \\ &= \frac{ip}{2\epsilon_0} \int \frac{d^2\mathbf{q}}{(2\pi)^2} e^{i\mathbf{k}\cdot\mathbf{R}} \left(1 + r(q, \omega) e^{2ik_{\perp}z_0} \right) \left(\mathbf{q} - \frac{q^2\hat{\mathbf{z}}}{k_{\perp}} \right), \end{aligned} \quad (\text{S36})$$

where $\mathbf{R} = \mathbf{r}_{\parallel} + (z - z_0)\hat{\mathbf{z}}$. To estimate the field measured by a detector placed far away from the tip-sample system, this integral may be evaluated in the asymptotic limit $R \rightarrow \infty$, where the integral is dominated by the stationary points where $\nabla_{\mathbf{q}}(\mathbf{k} \cdot \mathbf{R}) = 0$. Writing $\mathbf{k} \cdot \mathbf{R} = qr_{\parallel} \cos(\phi_q) + k_{\perp}(z - z_0)$, we get

$$\begin{aligned} \nabla_{\mathbf{q}} \mathbf{k} \cdot \mathbf{R} &= \left\{ \frac{\partial}{\partial q}, \frac{1}{q} \frac{\partial}{\partial \phi_q} \right\} [qr_{\parallel} \cos(\phi_q) + k_{\perp}(z - z_0)] \\ &= \left\{ r_{\parallel} \cos(\phi_q) - \frac{q}{k_{\perp}}(z - z_0), -r_{\parallel} \sin(\phi_q) \right\}, \end{aligned} \quad (\text{S37})$$

from which it follows, after some algebra, that $\nabla_{\mathbf{q}} \mathbf{k} \cdot \mathbf{R} = 0$ only if $\phi_q = 0, \pi$ and $q = kr_{\parallel}/R$, which are indeed the wavevectors parallel and antiparallel to \mathbf{R} . The only physical solution is then $q = kr_{\parallel}/R$ and $\phi_q = 0$, and we can write (up to a phase)

$$\mathbf{E}(\mathbf{r}, \omega) \approx \frac{ipe^{ikR}}{2\epsilon_0} \frac{1 + r[k \sin(\theta_{\text{out}}), \omega] e^{2ik \cos(\theta_{\text{out}}) z_0}}{\sqrt{|\det H|}} \left(\frac{k \sin(\theta_{\text{out}}) \mathbf{r}_{\parallel}}{r_{\parallel}} - \frac{k \sin^2(\theta_{\text{out}}) \hat{\mathbf{z}}}{\cos(\theta_{\text{out}})} \right), \quad (\text{S38})$$

where we defined $r_{\parallel} = R \cos(\theta_{\text{out}})$ and $z - z_0 = R \sin(\theta_{\text{out}})$. In this equation, H is the Hessian matrix

$$H = \begin{pmatrix} \frac{\partial^2(\mathbf{k} \cdot \mathbf{R})}{\partial q^2} & \frac{\partial^2(\mathbf{k} \cdot \mathbf{R})}{\partial q \partial \phi_q} \\ \frac{\partial^2(\mathbf{k} \cdot \mathbf{R})}{\partial q \partial \phi_q} & \frac{\partial^2(\mathbf{k} \cdot \mathbf{R})}{\partial \phi_q^2} \end{pmatrix} \quad (\text{S39})$$

and the determinant is evaluated at the stationary point. After some algebra, one obtains $\det H = R^2 \tan^2(\theta_{\text{out}})$ and

$$\mathbf{E}(\mathbf{r}, \omega) \approx \frac{ipe^{ikR}}{2\epsilon_0} \frac{1 + r[k \sin(\theta_{\text{out}}), \omega] e^{2ik \cos(\theta_{\text{out}}) z_0}}{R \tan(\theta_{\text{out}})} \left(\frac{k \sin(\theta_{\text{out}}) \mathbf{r}_{\parallel}}{r_{\parallel}} - \frac{k \sin^2(\theta_{\text{out}}) \hat{\mathbf{z}}}{\cos(\theta_{\text{out}})} \right). \quad (\text{S40})$$

From Eq. (S40) we get

$$E(\mathbf{r}, \omega) = \frac{ip_{\text{tot}} k e^{ikR}}{2\epsilon_0 R}, \quad (\text{S41})$$

where we defined

$$p_{\text{tot}} = p \left(1 + r(Q, \omega) e^{2ik_{\perp} z_0} \right) = \alpha_{\text{eff}} E_{\text{inc}, z} \left(1 + r(q, \omega) e^{2ik_{\perp} z_0} \right) \left(1 + r(Q, \omega) e^{2ik_{\perp} z_0} \right) \quad (\text{S42})$$

with $Q = k \sin(\theta_{\text{out}})$ and $K_{\perp} = k \sin(\theta_{\text{out}})$. For $\theta_{\text{out}} = \theta_{\text{inc}}$, as indicated in Fig. 1(d) and often convenient in s-SNOM setups [3–6], we can write

$$\begin{aligned} p_{\text{tot}} &= \alpha_{\text{eff}} E_{\text{inc}, z} \left(1 + r(q, \omega) e^{2ik_{\perp} z_0} \right)^2 \\ &= \alpha_{\text{eff}} E_{\text{inc}, z} \left(1 + r(q, \omega) \right)^2 + \mathcal{O}(k_{\perp} z_0). \end{aligned} \quad (\text{S43})$$

The demodulated components of the back-scattered field are then

$$\sigma_n = \frac{ik E_{\text{inc}, z} e^{ikR}}{2\epsilon_0 RT} \left(1 + r(q, \omega) \right)^2 \int_0^T dt e^{in\Omega t} \alpha_{\text{eff}}[z_0(t)], \quad (\text{S44})$$

for a tip-sample distance that oscillates in time with frequency Ω . We normalize these harmonics with respect to those of the pure substrate:

$$\bar{\sigma}_n = \frac{\left(1 + r(q_{\text{inc}}, \omega) \right)^2 \int_0^T dt e^{in\Omega t} \alpha_{\text{eff}}[z_0(t)]}{\left(1 + r_{\text{subs}}(q_{\text{inc}}, \omega) \right)^2 \int_0^T dt e^{in\Omega t} \alpha_{\text{eff,subs}}[z_0(t)]}, \quad (\text{S45})$$

as discussed in the main text. Fig. S1 compares the $s_n = |\bar{\sigma}_n|$ and $\varphi_n = \arg(\bar{\sigma}_n)$ for different incidence angles ranging from 0° to 90° . Two peaks are observed in $s_n = |\sigma_n|$ and $\varphi_n = \arg(\sigma_n)$, signaling the ability of s-SNOM to identify both modes (in-plane and out-of-plane) in the sheet. The modulus of the signal reaches up to 4 times that of the pure substrate, signaling a high quality contrast. As the incidence angle increases, the peaks are mildly diminished. In fact, as θ_{inc} increases the reflection of the polarization sheet decreases, damping the contrast of the signals. This reduction in contrast is not exceedingly large, thereby allowing for oblique incidence angles –as is often the case in s-SNOM setups [7, 8]– without much compromise in peak characterization. For the discussion in the main text, we fix a large incidence angle ($\theta_{\text{inc}} = 70^\circ$). Shorter incidence angles, if achievable experimentally, would lead to signals with even higher contrast than those shown in the main text.

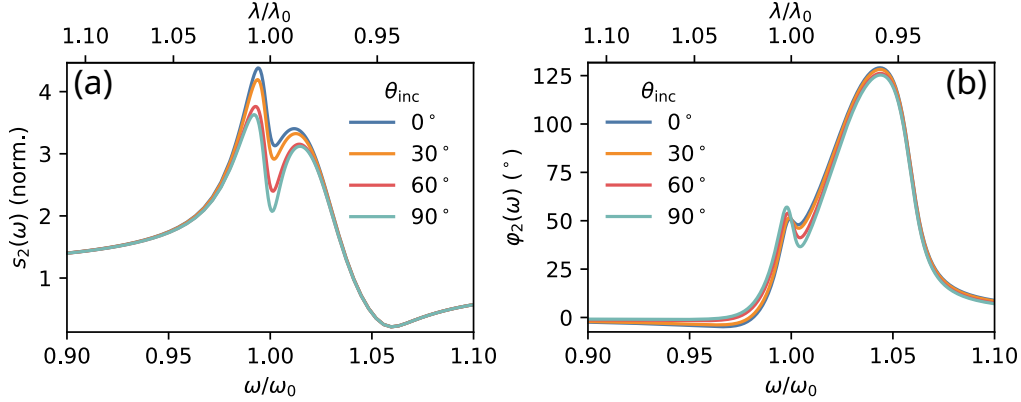


Fig. S1. (a) Modulus and (b) phase of 2nd harmonic demodulated signals of the scattered field of a polarization sheet on top of a substrate with $\mu_{\text{subs}}(\omega) = 1$ and $\epsilon_{\text{subs}}(\omega) = 2.25$, for $\theta_{\text{dip}} = 20^\circ$ and different incidence angles θ_{inc} .

3. FANO-LIKE RESONANCES IN NEAR-FIELD SPECTRA

As discussed in the main text, a Fano resonance can arise from the interaction of the polarization sheet with an s-SNOM tip. This Section provides additional information to support this claim.

The curve shapes shown in Fig. 4(a) of the main text can be fitted using a Fano line-shape function, written as

$$f(\omega) = a + m \frac{(\mathcal{E}(\omega) + q)^2}{\mathcal{E}^2(\omega) + 1}, \quad (\text{S46})$$

where q is the Fano asymmetry parameter, $\mathcal{E}(\omega) = (\omega - \omega_R)/\gamma$, and a , m , and ω_R are fitting parameters. In Fig. S2 we show in each panel the result for the fit obtained using the Fano function (S46). For $\theta_{\text{dip}} = 90^\circ$, the Fano function provides a fit in high agreement with the main resonance peak, confirming that the response follows a strongly asymmetric Fano profile [Fig. S2(a)]. For $\theta_{\text{dip}} = 60^\circ$ the agreement remains high, albeit slightly less pronounced due to a reduced out-of-plane coupling strength [Fig. S2(b)]. We verified that, for $\theta_{\text{dip}} = 5^\circ$, the agreement of the resulting Fano fit was noticeably lower, indicating that the coupling of the surface dipoles with the tip's point-dipole is only large enough for dipole angles θ_{dip} close to 90° .

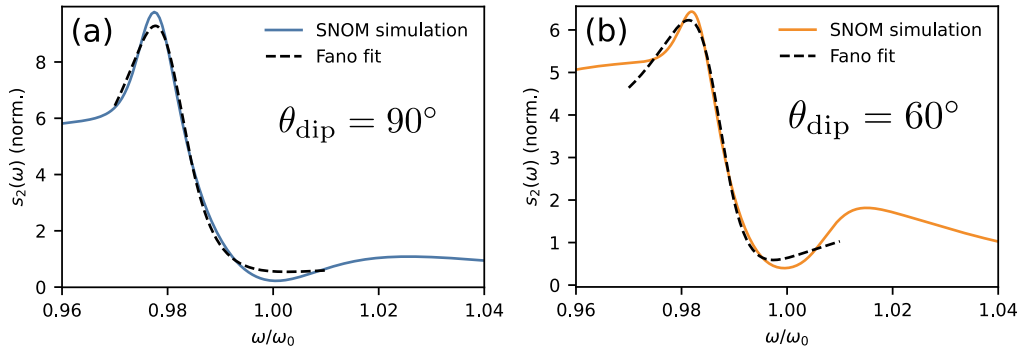


Fig. S2. Fits of the 2nd harmonic demodulated signals (s_2), normalized to substrate, for (a) $\theta_{\text{dip}} = 90^\circ$ and (b) $\theta_{\text{dip}} = 60^\circ$. The fitting function considered was Eq. (S46), with fitting parameters a , m , and ω_R .

To further confirm the occurrence of Fano-like resonances in the spectra, we performed numerical tests for different values of radius R_{tip} , including values artificially beyond physical and geometrical limitations imposed by the optical setup. By doing so, we verified that the asymmetry of the line shapes decreased significantly. For exceedingly large or small values of R_{tip} , the spectral features are completely lost, signaling that the resonant modes of the sample were no longer being properly excited. Decreasing the substrate permittivity down to $\epsilon_{\text{subs}} = 1.001$, effectively removing the substrate effect, the peaks became totally symmetric, indicating a minor

influence of the substrate as well on the asymmetric line shapes being observed in Fig. 4 of the main text.

4. NUMERICAL INTEGRATION

We use numerical integration to calculate the effective polarizability

$$\alpha_{\text{eff}} = \frac{\alpha}{1 - \alpha G}, \quad (\text{S47a})$$

$$G = \frac{i}{4\pi\epsilon_0} \int_0^\infty dq \frac{q^3}{k_\perp} e^{2ik_\perp z_0} r'_p(q, \omega), \quad (\text{S47b})$$

and the normalized field harmonics

$$\bar{\sigma}_n = \frac{(1 + r(q_{\text{inc}}, \omega))^2}{(1 + r_{\text{subs}}(q_{\text{inc}}, \omega))^2} \frac{\int_0^T dt e^{in\Omega t} \alpha_{\text{eff}}[z_0(t)]}{\int_0^T dt e^{in\Omega t} \alpha_{\text{eff,subs}}[z_0(t)]}. \quad (\text{S48})$$

For the former, we used adaptive Gaussian quadratures through the library Scipy of the Python programming language. The poles of the reflection coefficient are shifted away from the real line due to the damping parameter $\gamma \sim 0.01\omega_0$, so the adaptive quadrature safely handles its features. The remaining pole at $k_\perp = 0$ ($q = \omega/c$) is dealt by splitting the integral into the intervals $0 < q < (\omega/c)(1 - \epsilon)$ and $q > (\omega/c)(1 + \epsilon)$, for a sufficiently small tolerance parameter $\epsilon \ll 1$. The semi-finite interval is transformed into a finite one using $q = \omega/c(1 + \epsilon) + u/(1 - u)$ ($0 < u < 1$).

The integrals in (S48) are of the form

$$\frac{1}{T} \int_0^T dt e^{in\Omega t} f(\Omega t), \quad (\text{S49})$$

for some analytic function f , and can be straight-forwardly calculated using $t = n'T/N$ ($n' = 0, 1, 2, \dots, N - 1$):

$$\frac{1}{T} \int_0^T dt e^{in\Omega t} f(\Omega t) \approx \frac{1}{N} \sum_{n'=0}^{N-1} e^{i2\pi n n' / N} f(2\pi n n' / N), \quad (\text{S50})$$

for a sufficiently large number of points N . This shows that the integrals in Eq. (S48) do not depend on the tapping frequency Ω .

REFERENCES

1. B. Amorim, P. A. D. Gonçalves, M. I. Vasilevskiy, and N. M. R. Peres, "Impact of graphene on the polarizability of a neighbour nanoparticle: A dyadic Green's function study," *Appl. Sci.* **7**, 1158 (2017).
2. I. Pascual Robledo, C. Maciel-Escudero, M. Schnell, *et al.*, "Theoretical description of infrared near-field spectroscopy of in- and out-of-plane molecular vibrations in thin layers," *ACS Photonics* **12**, 3782–3793 (2025).
3. J. Aizpurua, T. Taubner, F. J. García de Abajo, *et al.*, "Substrate-enhanced infrared near-field spectroscopy," *Opt. Express* **16**, 1529–1545 (2008).
4. T. Taubner, F. Keilmann, and R. Hillenbrand, "Nanomechanical resonance tuning and phase effects in optical near-field interaction," *Nano Lett.* **4**, 1669–1672 (2004).
5. N. Ocelic, A. Huber, and R. Hillenbrand, "Pseudoheterodyne detection for background-free near-field spectroscopy," *Appl. Phys. Lett.* **89**, 101124 (2006).
6. A. Cvitkovic, N. Ocelic, and R. Hillenbrand, "Analytical model for quantitative prediction of material contrasts in scattering-type near-field optical microscopy," *Opt. Express* **15**, 8550–8565 (2007).
7. T. Neuman, P. Alonso-González, A. Garcia-Etxarri, *et al.*, "Mapping the near fields of plasmonic nanoantennas by scattering-type scanning near-field optical microscopy," *Laser & Photonics Rev.* **9**, 637–649 (2015).
8. X. Chen, D. Hu, R. Mescall, *et al.*, "Modern scattering-type scanning near-field optical microscopy for advanced material research," *Adv. Mater.* **31**, 1804774 (2019).